grow. In the meantime, the two Voyager spacecraft will continue to explore the interplanetary medium, perhaps encountering the heliopause. If the spacecraft continue to operate as well in the future as they have in the past, they might continue to transmit data until well into the 21st century, when their radioisotope thermoelectric power output will eventually drop to levels that are insufficient to permit spacecraft operation.

REFERENCES AND NOTES

1. For a discussion of the spacecraft, mission design criteria, trajectory selection, and the scientific investigations, see *Space Sci. Rev.* **21**, 75 (1977); *ibid.*, p. 235. A description of the design of the Voyager spacecraft is given in R. F. Draper, W. I. Purdy, G. Cunningham, paper 75-1155 presented at the American Institute of Aeronautics and Astronautics–American Geophysical Union Conference on the Exploration of the Outer Planets, St. Louis, MO, 17–19 September 1975.
2. Voyager 1 Jupiter results are outlined in *Science* **204**, 945–1008 (1979); *Nature (London)* **280**, 725–806 (1979); *Geophys. Res. Lett.* 7, 1–68 (1980). Voyager 2 Jupiter results are outlined in *Science* **206**, 925–996 (1979). Combined Voyager Jupiter results are contained in *J. Geophys. Res.* **85**, 8123—8841 (1981).
3. Voyager 1 Saturn results are outlined in *Science* **212**, 159–243 (1981); *Nature (London)* **292**, 675–755 (1981). Voyager 2 Saturn results are outlined in *Science* **215**, 499–594 (1982). Combined Voyager Saturn results are contained in *J. Geophys. Res.* **88**, 8625–9018 (1983). See also two special Saturn issues of *Icarus* [**52**, no. 2 (1983); **54**, no. 2 (1983)]; T. Gehrels and M. S. Matthews, Eds., *Saturn* (Univ. of Arizona Press, Tucson, 1984); R. Greenberg and A. Brahic, Eds., *Planetary Rings* (Univ. of Arizona Press, Tucson, 1984).
4. R. G. French, J. L. Elliot, E. E. Levine, in preparation.

5. We wish to pay special tribute to the members of the Voyager project team, without whom the data reported in these papers could not have been collected. The Voyager program is one of the programs of the Solar System Exploration Division of NASA's Office of Space Science and Applications. The Voyager project is managed by the Jet Propulsion Laboratory of the California Institute of Technology under NASA contract NAS7-918.

14 April 1986; accepted 5 May 1986

Voyager 2 in the Uranian System: Imaging Science Results

B. A. SMITH, L. A. SODERBLOM, R. BEEBE, D. BLISS, J. M. BOYCE, A. BRAHIC, G. A. BRIGGS, R. H. BROWN, S. A. COLLINS, A. F. COOK II, S. K. CROFT, J. N. CUZZI, G. E. DANIELSON, M. E. DAVIES, T. E. DOWLING, D. GODFREY, C. J. HANSEN, C. HARRIS, G. E. HUNT, A. P. INGERSOLL, T. V. JOHNSON, R. J. KRAUSS, H. MASURSKY, D. MORRISON, T. OWEN, J. B. PLESCIA, J. B. POLLACK, C. C. PORCO, K. RAGES, C. SAGAN, E. M. SHOEMAKER, L. A. SROMOVSKY, C. STOKER, R. G. STROM, V. E. SUOMI, S. P. SYNNOTT, R. J. TERRILE, P. THOMAS, W. R. THOMPSON, J. VEVERKA

Voyager 2 images of the southern hemisphere of Uranus indicate that submicrometer-size haze particles and particles of a methane condensation cloud produce faint patterns in the atmosphere. The alignment of the cloud bands is similar to that of bands on Jupiter and Saturn, but the zonal winds are nearly opposite. At mid-latitudes (−70° to −27°), where winds were measured, the atmosphere rotates faster than the magnetic field; however, the rotation rate of the atmosphere decreases toward the equator, so that the two probably corotate at about −20°. Voyager images confirm the extremely low albedo of the ring particles. High phase angle images reveal on the order of 10^2 new ringlike features of very low optical depth and relatively high dust abundance interspersed within the main rings, as well as a broad, diffuse, low optical depth ring just inside the main ring system. Nine of the newly discovered small satellites (40 to 165 kilometers in diameter) orbit between the rings and Miranda; the tenth is within the ring system. Two of these small objects may gravitationally confine the ϵ ring. Oberon and Umbriel have heavily cratered surfaces resembling the ancient cratered highlands of Earth's moon, although Umbriel is almost completely covered with uniform dark material, which perhaps indicates some ongoing process. Titania and Ariel show crater populations different from those on Oberon and Umbriel; these were probably generated by collisions with debris confined to their orbits. Titania and Ariel also show many extensional fault systems; Ariel shows strong evidence for the presence of extrusive material. About half of Miranda's surface is relatively bland, old, cratered terrain. The remainder comprises three large regions of younger terrain, each rectangular to ovoid in plan, that display complex sets of parallel and intersecting scarps and ridges as well as numerous outcrops of bright and dark materials, perhaps suggesting some exotic composition.

VOYAGER 2 ACQUIRED APPROXIMATELY 7000 images of Uranus, its rings, and its satellites during the several months surrounding the spacecraft's closest approach to Uranus in late January 1986. Images of the Uranian system were more difficult to acquire than those of Jupiter and Saturn for several reasons. Because of the low light levels [Uranus is about 19 astronomical units (AU) from the sun], long exposures and complex sequences to compensate for image motion were required to obtain high-quality satellite images (most notably those of Miranda). Spacecraft engineering teams also redesigned the spacecraft's attitude control software to reduce random spacecraft motion. Image data compression was introduced to compensate for the low telemetry rates resulting from the large transmission distances. All of these efforts were successful and yielded many unsmeared, long-exposure images rich in details of the atmosphere and rings that would otherwise have remained unseen; they also provided some of the highest quality and highest resolution images of satellite surfaces acquired during any of the five Voyager encounters.

The Atmosphere of Uranus

Uranus is a low-contrast object. Variations in lighting and viewing angles cause about 95% of the brightness variation across the planet. Only after this dominant component is removed do the images reveal the underlying patterns that contain the fine

B. A. Smith, S. K. Croft, C. C. Porco, R. G. Strom, University of Arizona, Tucson, AZ 85721.
L. A. Soderblom, H. Masursky, J. B. Plescia, E. M. Shoemaker, U.S. Geological Survey, Flagstaff, AZ 86001.
R. Beebe, New Mexico State University, Las Cruces, NM 88003.
D. Bliss, R. H. Brown, S. A. Collins, C. J. Hansen, T. V. Johnson, S. P. Synnott, R. J. Terrile, Jet Propulsion Laboratory, California Institute of Technology, Pasadena, CA 91109.
J. M. Boyce and G. A. Briggs, NASA Headquarters, Washington, DC 20546.
A. Brahic, Observatoire de Paris, Meudon, Paris, France.
A. F. Cook II, Center for Astrophysics, Cambridge, MA 02138.
J. N. Cuzzi, J. B. Pollack, K. Rages, C. Stoker, NASA Ames Research Center, Moffett Field, CA 94035.
G. E. Danielson, T. E. Dowling, A. P. Ingersoll, California Institute of Technology, Pasadena, CA 91125.
M. E. Davies, Rand Corporation, Santa Monica, CA 90406.
D. Godfrey, C. Harris, G. E. Hunt, Imperial College, London, England.
R. J. Krauss, L. A. Sromovsky, V. E. Suomi, University of Wisconsin, Madison, WI 53706.
D. Morrison, University of Hawaii, Honolulu, HI 96822.
T. Owen, State University of New York, Stony Brook, NY 11794.
C. Sagan, P. Thomas, W. R. Thompson, J. Veverka, Cornell University, Ithaca, NY 14853.

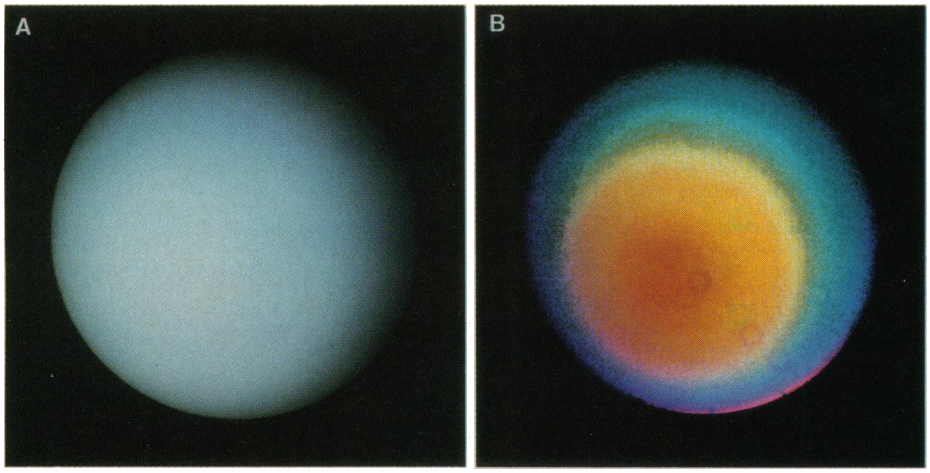

Fig. 1. Views of Uranus without (A) and with (B) enhancement. (A) Color composite produced from blue, green, and orange images acquired with the narrow-angle camera. The color balance was adjusted to stimulate the view the eye would normally see. The phase angle is 14°; the resolution is 160 km per line pair. (B) The average of two ultraviolet images was used for blue, the average of a violet image and a blue image for green, and the average of a green image and an orange image for red. A Minnaert photometric model (*1*) was used to suppress the overall brightness gradient away from the subsolar point (see text). Both the color and the brightness contrast have been greatly exaggerated. The doughnut-shaped features are artifacts caused by dust in the narrow-angle camera optics.

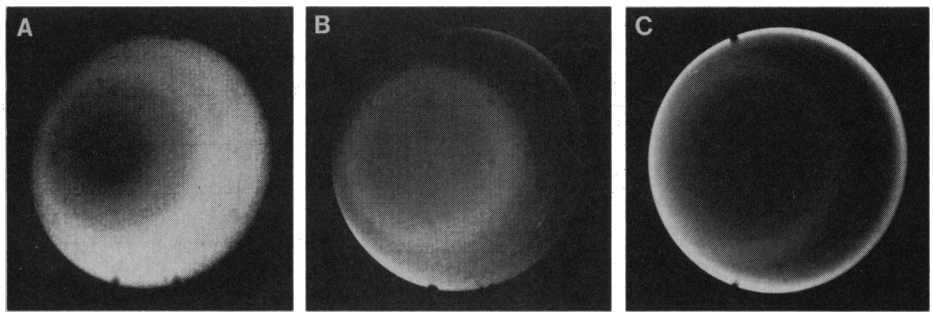

Fig. 2. Contrast-enhanced wide-angle images of Uranus acquired through the violet filter (A), orange filter (B), and methane filter (0.619 μm) (C). The phase angle is 17°; the resolution is 300 km per line pair. Shown are the ratios of brightness in the original images to that modeled with a Minnaert photometric function (*1*) with $k = 0.8$. Contrast in the processed image has been stretched to bring out atmospheric features. The concentric banding is centered on the pole of rotation, not on the subsolar point. [Image processing by L. A. Wainio]

structure, color variations, and organization about directions that are different from the subsolar-antisolar axis.

Figure 1A shows a Voyager image of Uranus' sunlit southern hemisphere with approximately the color that the human eye would see and without contrast enhancement. The blue-green color is due to the selective absorption of long wavelengths by methane gas in the planet's atmosphere. The dominant structure is the falloff of brightness away from the subsolar point, which lies slightly to the left of center. To remove this structure we divided the signal by a Minnaert photometric function (*1*), in which brightness is proportional to $\mu_0 \mu^{k-1}$, where μ_0 and μ are the cosines of the incidence and emission angles, respectively (Fig. 1B). Figures 2 and 3 show sets of violet, orange, and methane (0.619 μm) images in which a Minnaert function was similarly removed and the residual contrast was stretched. The constant k was chosen to minimize these large-scale brightness variations; no physical significance is attached to the choice of a Minnaert function or to the value of k. Discrete features and large-scale banding concentric around the pole of rotation can be seen in the collection of enhanced images. Figure 4, A and B, compares equator-to-pole brightness profiles across images obtained through eight of the narrow- and wide-angle camera filters; these profiles were also normalized to Minnaert functions. Experimenting with values of k from 0.65 to 0.85 revealed that the structure equatorward of −10° latitude is unreliable. Real aspects of the data include the dark polar cap poleward of −80° in the violet image (VN and VW in Fig. 4), the brightness maximum around −50° in most images, and the brightness minima at −30°

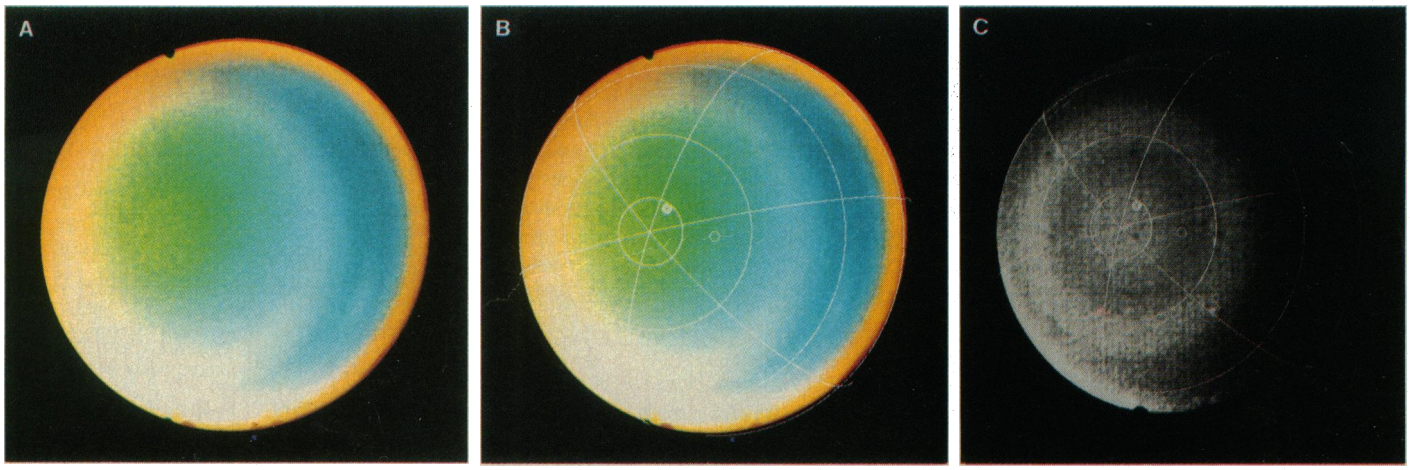

Fig. 3. Color composite of the three contrast-enhanced images of Fig. 2. (A) The violet, orange, and methane images were combined as blue, green, and red in this false-color version. The violet-absorbing haze over the polar region appears green, the mid-latitude cloud appears white, the low-latitude region of depressed cloud appears blue, and the limb haze appears orange. (B) The image in (A) was overlain with a planetocentric latitude-longitude grid. The subsolar point is indicated by a filled circle and the subspacecraft point by an open circle. (C) This image was constructed from the ratio of an orange image to a blue image. It shows most clearly that the banding is centered on the pole of rotation and not on the subsolar point.

and −65° and the limb brightening equatorward of −20° in the 0.619-μm methane-filter image. All but the two methane-filter images are calibrated in absolute units (*2*), so that the model reflectances given on the ordinate in Fig. 4 are meaningful in all but these two cases. The crossing of the blue (BL) and green (GR) curves by the violet curve in Fig. 4 is also real.

Cloud structure. Earth-based spectroscopic observations (*3, 4*) provide useful constraints on models of the vertical structure of the atmosphere. Voyager radio science observations (*5*) and infrared observations (*6*) provide estimates of the vertical temperature structure, the hydrogen-helium ratio, and the methane abundance. These models help us interpret the brightness variations in the Voyager images. At pressures less than about 1 bar, sunlight is Rayleigh-scattered by hydrogen molecules and helium atoms and is scattered and absorbed by a photochemically produced haze. At greater depths it interacts at selected wavelengths with gaseous methane and at all wavelengths with the particles of a methane condensation cloud whose base, according to Voyager RSS observations (*5*), is at 1.3 bar. The abundance of methane gas decreases rapidly with altitude above the cloud base, so that the gas absorbs preferentially in the region of the clouds. The optical depth of gas plus haze is greatest at short wavelengths. The combined Rayleigh scattering and haze optical depth at 1 bar is of order 2 in violet light and of order 0.5 in orange light. Because the haze absorbs better than the gas at short wavelengths, increases in the amount of haze relative to gas show up as brightness decreases in the short-wavelength–filter images. Conversely, because the methane gas absorbs more effectively than the haze at long wavelengths, increases in the haze relative to gas show a brightness increase in the long-wavelength–filter images. A dark feature shows up in the methane-filter image (0.619 μm) but not in the orange image (with a broader bandpass and an effective wavelength of 0.614 μm); this feature indicates a thinning of the deep condensation cloud, not of the upper haze layer.

We interpret the relative darkness of the polar region in violet light as an indication of a large abundance of violet-absorbing haze particles. The dark feature is centered on the axis of rotation (as defined by satellite and ring orbits) and has a radius about 10° in latitude (Fig. 3). The feature is offset from the subsolar point, which lies 8° of latitude away from the pole of rotation. This symmetry around the pole of rotation indicates that the atmospheric circulation affects the haze distribution. Figure 4 shows that the polar feature is most conspicuous in images taken by the narrow-angle camera through the violet filter. This filter has an effective wavelength (0.413 μm) only slightly shorter than that of the violet filter of the wide-angle camera (0.431 μm). That the narrow-angle camera's violet curve crosses the other curves (Fig. 4) is further evidence that the haze absorbs selectively at this wavelength. We interpret the band at −45° to −55° latitude that is relatively bright at long wavelengths to be a region of well-developed clouds and haze. The contrast between this band and those on either side of it is greatest in the 0.619-μm methane-filter image, suggesting that variations are taking place at least down to 1 bar. The band from −20° to −40° latitude is bright in violet and dark in methane-filter images, suggesting a region of depressed clouds and thinner haze. Discrete features and banded structures are visible within this band, especially in the long-wavelength images. The location of this band coincides with that of a 2-K temperature minimum observed in the Voyager IRIS pole-to-pole scan (*6*). Those data show average brightness temperatures between pressures of 0.4 and 0.9 bar, a layer thought to be somewhat above the discrete methane clouds visible in the images. Although the magnetic pole of Uranus is within this band, we see no way that electromagnetic forces could be important in the neutral atmosphere to which our data refer.

The association between depressed clouds and low temperatures in the upper troposphere is the opposite of the association at Jupiter (*7*). Depressed clouds in Jupiter's atmosphere have been explained as a sign of sinking motion: sinking brings gas with a higher potential temperature down from higher altitudes, leading to higher temperatures at constant pressure. The explanation defies the notion that hot air rises, but it should apply in regions removed from the sources and sinks of energy. For Uranus, one could argue that the sources and sinks of energy are close at hand. Latent heat release in a hydrogen-helium atmosphere containing 2% methane produces a temperature change of 6 or 7 K. Latitudinal variations in the amount of methane could therefore account for the temperature variations measured by Voyager IRIS. On Jupiter the visible cloud is ammonia; its abundance is only 0.02%, and its latent heat effects are negligible.

The enhanced methane image (Fig. 2) shows a conspicuous brightening close to the planet's limb. Because the raw image faintly displays the same pattern, we conclude that this limb brightening is real, not simply an artifact of the processing. The rapid decline of the gaseous methane mixing ratio with altitude above the base of the methane condensation cloud at least partly causes the brightening. The scattered pho-

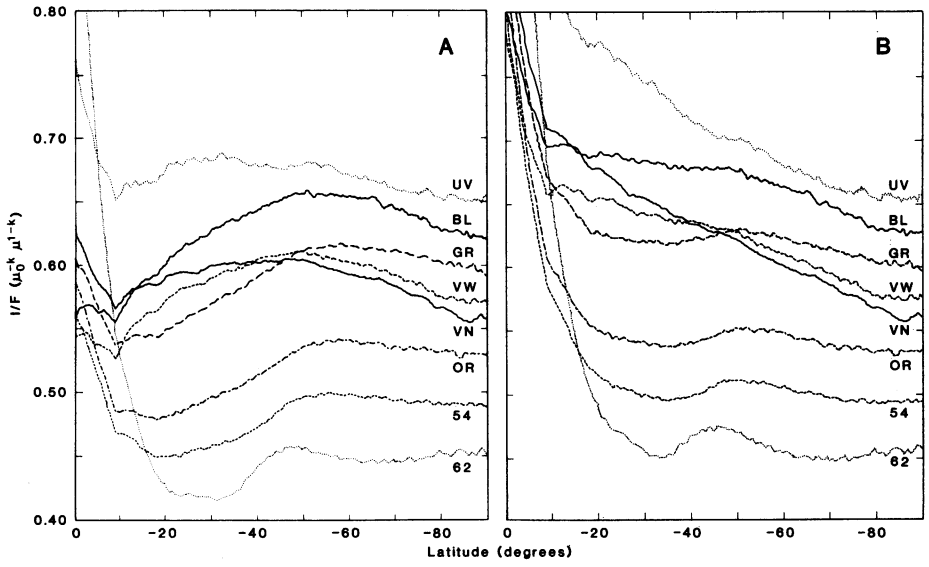

Fig. 4. Brightness of Uranus as a function of planetocentric latitude. Symbols and effective wavelengths for the narrow-angle camera filters: UV, ultraviolet (0.351 μm); VN, violet (0.413 μm). Symbols and effective wavelengths for the wide-angle camera filters: VW, violet (0.431 μm); BL, blue (0.477 μm); GR, green (0.572 μm); OR, orange (0.614 μm); 54, methane-1 (0.541 μm); 62, methane-2 (0.619 μm). Each image (or average of two images for the ultraviolet) was radiometrically calibrated in units of *I/F* (*2*) and then divided by a Minnaert photometric function (*1*) with $k = 0.7$ (A) and $k = 0.8$ (B). Profiles were extracted along the central meridian, averaging over 1° in latitude by 10° in longitude. Except for the two methane filters, for which calibration data are not available, the reflectivities are generally accurate to 5% (10% for the ultraviolet). The phase angles vary from 14° to 17°, with resolutions of approximately 170 km per line pair (300 km per line pair for the two methane-filter images). [Image processing by D. A. Alexander]

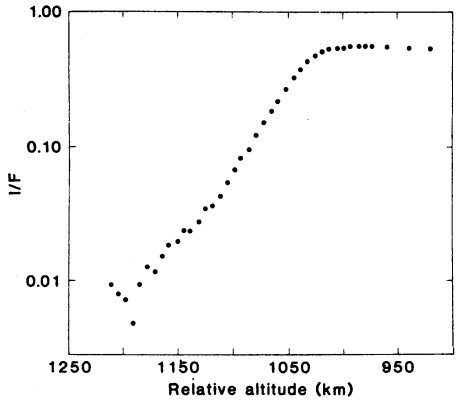

Fig. 5. Profile of brightness near the limb of Uranus derived from a narrow-angle image with a phase angle of 157° and a resolution of 12.5 km per line pair. Distance above the limb is given along the abscissa; the origin on this scale is arbitrary.

tons originate from higher altitudes in regions close to limb and terminator than in regions closer to the center of the disk. Therefore, near the limb photons experience less absorption by gaseous methane. Limb brightening could also be caused by higher concentrations of haze particles (scatterers) at low latitudes, because these latitudes are visible near the limb and terminator in Fig. 2.

Two elongated, bright features at −27° and −35° latitude can be seen in the orange filter image of Fig. 2 (lower right and upper left parts of the disk, respectively). These features may represent places where the methane cloud is at higher elevation as a result of increased convective activity. They appear bright at long wavelengths because less methane is absorbed before sunlight is reflected back into space. The contrast of these features relative to their surroundings is shown in Table 1. We have attempted to estimate the altitude difference between these discrete features and their surroundings by comparing their contrast as seen in orange, green, and methane-filter (0.619-μm) images. Images in orange and green were used to estimate the contrast of the features in the continuum at the effective wavelength of the methane-filter image; the additional contrast measured in the methane-filter image was considered due solely to differential absorption by gaseous methane above the feature compared to its surroundings (*8*). To estimate a differential altitude from the inferred differential absorption, we assumed that gaseous methane follows its saturation vapor-pressure curve in the vicinity of the clouds. The values assumed for scattering and absorption by haze above 1 bar are consistent with Earth-based observations (*3, 4*) and with Voyager images at high phase angles. We deduced that the clouds in question are several kilometers above those in their surroundings.

Haze properties. Observations of the planet's limb at high phase angles are particularly useful for defining the physical and geometrical properties of the haze because sunlight scattered out of the atmosphere at these oblique angles penetrates only to the region above the clouds. Also, the submicrometer- to micrometer-sized particles that typically constitute the haze in the atmospheres of the outer planets scatter sunlight preferentially at small scattering angles (high phase angles). Images at different wavelengths and phase angles allow the relative contributions of gas and haze to the extinction of sunlight and also the mean particle radius of the haze to be determined. The peak brightness of the planet near its limb increases by 10% from a phase angle of 148° to 157° when observed through the clear filter of the narrow-angle camera (effective wavelength, 0.477 μm). The uncertainty in this brightness increase is 2%. For comparison, the peak brightness of an optically thick, pure Rayleigh-scattering atmosphere would decrease by about 15% over this same range of phase angles. These data show that haze particles exist in the region above the clouds (above 1 bar). The latitudinal variation of the planet's brightness in the violet images, as discussed above, is a further demonstration.

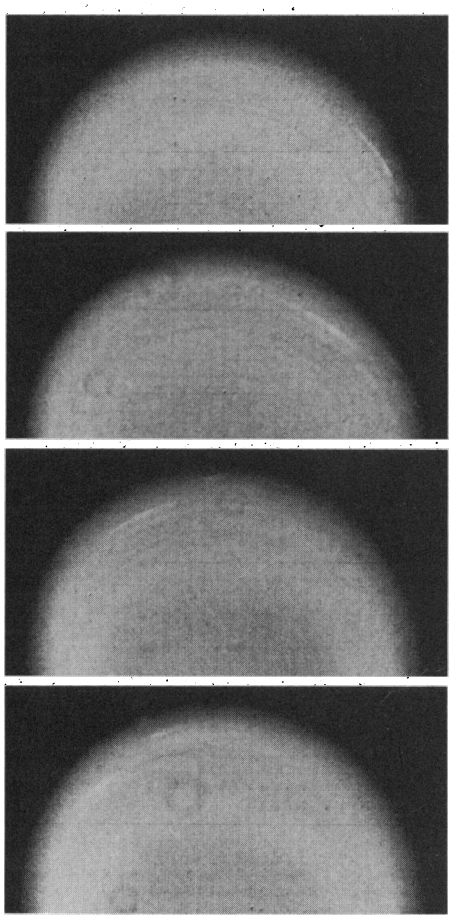

Fig. 6. Time-lapse sequence of four narrow-angle orange-filter images, showing small-scale bands and discrete features at latitudes from −25° to −40°. The counterclockwise rotation is clearly visible in this 4.6-hour sequence. The resolution is 230 km per line pair.

Table 1. Contrast (in percent) of discrete atmospheric features at latitudes of −27° and −35°.

Filter	Wavelength (μm)	Latitude	
		−27°	−35°
Violet	0.431		<1.0
Blue	0.477		1.2 ± 0.4
Green	0.572	3.5 ± 0.5	2.0 ± 0.5
Orange	0.614	3.6 ± 0.5	2.2 ± 0.2
Methane	0.619	6.9 ± 0.5	4.3 ± 0.4

For the haze, the observed phase angle brightening is determined chiefly by the shape of the diffraction peak of the particles (*9*). In turn, this diffraction pattern is determined chiefly by the mean size of the particles. We modeled these data using a radiative transfer code that incorporates the spherical geometry near the planet's limb for sunlight that is singly scattered out of the atmosphere; the code includes a correction for multiply scattered light for a nearly equivalent, plane-parallel atmosphere of gas plus haze (*9*). We did not consider variations in haze properties with latitude, although different latitudes are sampled at different phase angles. Comparison of the model results with the observed phase angle brightening implies that the average particle radius, weighted by the cross section, lies between 0.25 and 0.35 μm at a pressure of tens of millibars. This level was estimated from the vertical optical depth (0.03) of the limb position used, the molecular Rayleigh-scattering optical depth's dependence on pressure, and our estimate of the ratio (0.1 to 0.3) of haze to molecular extinction (*4*).

Images of the limb at high spatial resolution allow the vertical distribution of the haze to be determined, provided that the contribution of the gas can be separated out. Figure 5 shows a brightness profile across the planet's limb at −23° latitude and a phase angle of 157°. The profile was derived from a clear-filter image with a resolution of 12.5 km per line pair; the exposure was 0.72 second, and the smear was less than 1 pixel. The resolution is therefore less than the atmospheric scale height of about 30 km. The altitude in Fig. 5 is relative, but from whole-disk imaging we estimate that the planet's visible equatorial radius is 25,600 to 25,700 km. These values are consistent with those derived from Earth-based stellar occultations (*10*). The sloping parts of the curve in Fig. 5 have scale heights of 47 km

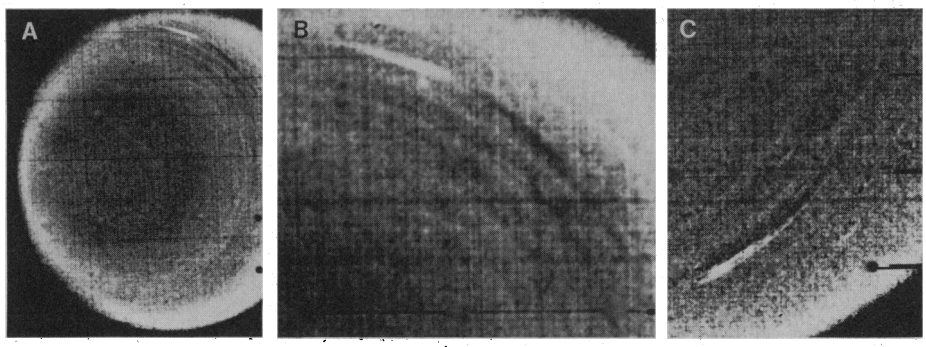

Fig. 7. (A) Convective plume at −35° planetocentric latitude. The plume tails extend in the positive zonal direction (the direction of rotation, which is counterclockwise in this image). (B) Enlargement (×3) of part of the image in (A). (C) The same feature shown 10 hours later at the same scale as in (B).

in the regions above the relative altitude of 1115 km and 27 km in the regions below this altitude. These scale heights are close to those expected for the gas at the pressures to which these data refer—0.1 to 10 mbar (*5, 6*). There are two possibilities: either the gas and haze are uniformly mixed, or the haze is absent at these high altitudes.

Very long exposures of the dark side of Uranus, taken while the spacecraft was in the planet's shadow, did not reveal evidence of lightning or aurora. Faint features may be found after further processing, when all spurious effects of the camera system have been removed.

Circulation patterns. The cloud patterns and the cloud motions both reveal a dominantly zonal circulation—one that is symmetric about the axis of rotation with winds blowing east-west rather than north-south. The dominance of zonal motions is also characteristic of Jupiter, Saturn, Venus, and, to a lesser extent, Earth and Mars. That all these circulation systems are zonal, despite the various patterns in the solar-heating distribution, attests to the importance of rotation in atmospheric circulations. Uranus is the only planet whose poles receive more sunlight than its equator; yet, as on other planets, the winds follow circles of constant latitude as defined by the pole of rotation. Figure 6 shows details of the circulation in a time-lapse sequence.

The spacing of the atmospheric bands is a strong function of latitude. Poleward of −45°, where we see primarily the haze layer, there are gradual changes in color and intensity (Figs. 2 and 3). From −45° to −20° latitude a reduction in the haze allows sunlight to penetrate to deeper levels, where appreciable amounts of methane gas are found. Here the bands are more numerous, with at least four complete cycles of bright and dark from −41° to −35° latitude (Fig. 6). The latitudinal wavelength, about 700 km, is thus considerably smaller than that for Jupiter and Saturn (*7, 11*). For Jupiter we tracked thousands and for Saturn hundreds of features and thereby deduced the latitudinal profile of zonal (east-west) velocity in considerable detail; generally the spacing of the visible bands is comparable to the wavelength of variations in the zonal velocity profile. For Uranus we have no information about the zonal velocity profile on scales as small as the band spacing. The zonal velocity profile may be smooth on these small scales. If the profile is smooth, the narrow bands could represent the outflow from a number of isolated disturbances that move zonally with respect to the visible mean cloud layer, perhaps because the mean cloud layer and the disturbances are at different altitudes.

Figure 7 provides support for the above hypothesis. The bright feature in the image is at −35° planetocentric latitude, in the sunlit hemisphere. It consists of a bright nucleus and a long tail or pair of tails that extend along latitude circles in the direction of the planet's rotation, which we shall call the positive zonal direction. Because clouds usually form on updrafts, the nucleus of the bright feature is probably centered over a source of cloud material that lies at a lower altitude than the tails. The positive orientation of the tails relative to the nucleus implies that the zonal wind becomes more positive with altitude. This interpretation holds only for this latitude and altitude (at a pressure of about 1 bar according to the earlier discussion). It implies that the narrow spacing of the Uranian cloud bands from −45° to −20° latitude is a consequence of the narrowness of the source regions and the low rate of lateral diffusion in the clouds.

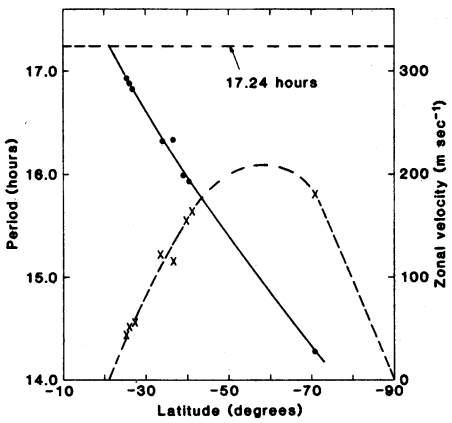

Fig. 8. Measured zonal velocities for the southern hemisphere as a function of planetocentric latitude. The points connected by the solid curve are rotation periods determined from individual spot motions. The error is less than 0.1 hour in all cases. The points connected by the dashed curve are the corresponding zonal velocities relative to the 17.24-hour period of the magnetic field (*12*). The point at −70° was obtained from violet images and may therefore refer to a higher altitude than the other points, which were obtained from orange images.

The feature at −35° was observed for 15 rotations (~10 days) until the spacecraft passed behind the planet. This feature was accompanied by a secondary nucleus, positioned at a slightly higher latitude, that traveled with the main feature (Fig. 7). A similar feature at −27° planetocentric latitude was observed for 14 rotations. The feature at −35° almost lapped the one at −27°; the former traveled more than half the planet's circumference relative to the latter during the 10-day interval. The periods of rotation for these two features are 16.3 and 16.9 hours, respectively. These periods were calculated by averaging over the longest time intervals for which the features were observed.

Smaller transient features were observed near −40° latitude. Several of these persisted for 1 day or more, allowing the local rotation period to be determined. The analysis was done separately at the Jet Propulsion Laboratory and at the University of Wisconsin by means of programs that had been used to track features on Jupiter and Saturn (*11*). Figure 8 shows the result of the tracking analysis. The periods for the features at −27° and −35° agree with those derived from long-term averaging. The rotation period near −40° is about 16.0 hours. A feature at −70° was tracked for more than 6 days in narrow-angle violet images. Its rotation period is 14.2 hours. Because the haze thickness varies with latitude and because the feature at −70° was observed only in violet, its altitude may be different (perhaps higher) than features at lower latitudes.

Winds. Figure 8 also shows the positive wind speed relative to the 17.24-hour rotation period of the magnetic field as determined by Voyager PRA and MAG observations (*12*). At these latitudes and altitudes, the atmosphere rotates faster than the planet's interior. The results of extrapolation suggest that the zonal velocity profile reaches zero at about −20° latitude; it seems

to reach a maximum around −50° or −60° latitude. Although angular velocity increases with increasing latitude, angular momentum per unit mass decreases with increasing latitude. For comparison, in a nearly inviscid, zonally symmetric (Hadley) circulation, the angular momentum per unit mass is independent of latitude. Finally, the trend of Fig. 8 suggests that the atmosphere rotates more slowly than the magnetic field within 20° of the equator. An equatorial subrotation of this sort was predicted by Read (*13*) from models of axisymmetric circulations. He argued that the circulation should be from pole to equator at high altitudes on Uranus and should therefore maintain the equatorial upper atmosphere in a low angular momentum state relative to the interior.

The orientation of plume tails (Fig. 7) and the evidence of positive winds relative to the interior (Fig. 8) both suggest that zonal velocity increases with altitude, at least in the band from −27° to −70° latitude. Such an increase is surprising. The thermal wind equation of meteorology (*14*) states that the increase (or decrease) of zonal velocity with altitude is proportional to the increase (or decrease) of density with latitude. The change in density is measured at constant pressure, so that temperature is commonly used as an inverse measure of density. If density were controlled by temperature, the latter would have to decrease toward the pole at the altitude and latitude of the plume (1 bar, −35°). This inference contrasts with the temperature increase with latitude measured by Voyager IRIS (*6*) at the same latitude but at somewhat higher altitudes (pressures of 0.4 to 0.9 bar). A poleward temperature decrease also violates expectations based on radiative heating of the atmosphere by sunlight. Density may also increase with latitude as a result of molecular weight variation—a possible consequence of methane condensation. We have no simple explanations and therefore conclude that dynamical processes are creating a more complicated density distribution than that predicted from radiative equilibrium and constant composition alone.

This conclusion is reinforced when one applies the thermal wind equation to the measured zonal velocities (Fig. 8), which were moving in a positive direction relative to the interior as revealed by the magnetic field. The interpretation is complicated be-

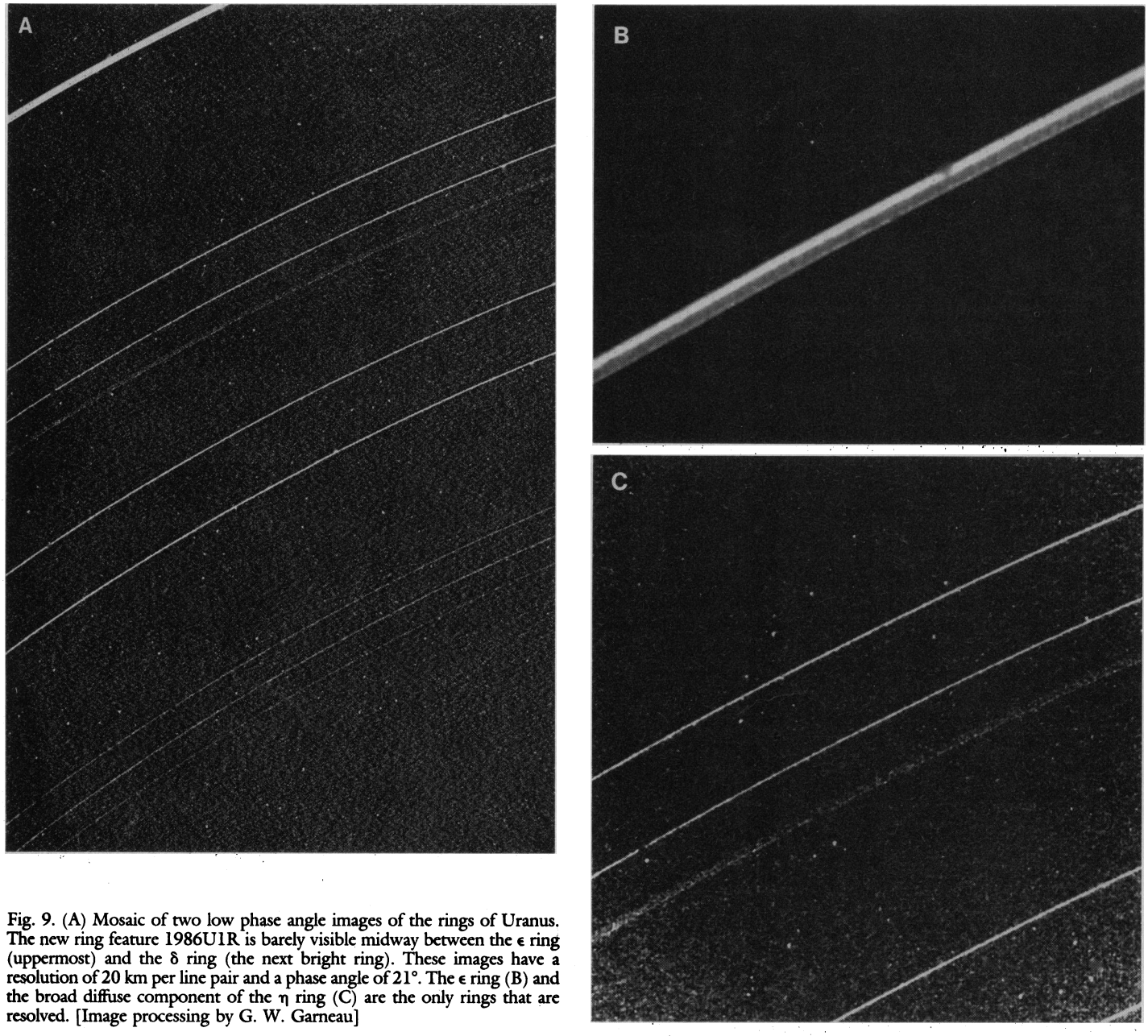

Fig. 9. (A) Mosaic of two low phase angle images of the rings of Uranus. The new ring feature 1986U1R is barely visible midway between the ϵ ring (uppermost) and the δ ring (the next bright ring). These images have a resolution of 20 km per line pair and a phase angle of 21°. The ϵ ring (B) and the broad diffuse component of the η ring (C) are the only rings that are resolved. [Image processing by G. W. Garneau]

cause we are uncertain of the depth below which the interior must corotate with the magnetic field. This depth depends on the electrical conductivity of the interior, but it could be a substantial fraction (10% to 30%) of the planet's radius (*15*). There are two possibilities, depending on the thickness of the spherical shell of fluid that lies between the visible clouds and the corotating sphere. If the shell is thin—of order 10% of the radius—then the results of Fig. 8 imply that density increases from equator to pole within the shell. There is no obvious reason to expect such a density increase, however. If the shell is thick—of order 30% of the radius—then only the single point at −70° provides any information about the density distribution. Points at lower latitudes are irrelevant because the thermal wind equation involves only the change of zonal velocity parallel to the axis of rotation (*16*) and therefore allows cylinders of fluid, concentric about the axis of rotation, to rotate separately. Those cylinders that do not intersect the corotating sphere may rotate at any rate (at least their rates do not involve the density distribution). Thus the full implications of the results shown in Fig. 8 depend on a better knowledge of the electrical conductivity of the interior and the depth of the corotating sphere.

The Uranian Rings

Earth-based stellar-occultation observations of the Uranian rings have been until now the dominant source of our knowledge of this distant ring system (*17*). Analysis of these near infrared observations indicated the existence of nine narrow, sharp-edged rings of relatively high optical depth ($\tau \geq 0.3$). In order of increasing orbital radius from the center of Uranus, they have been unofficially referred to as the 6, 5, 4, α, β, η, γ, δ, and ϵ rings. All but the η ring are eccentric; all but the η, γ, and ϵ rings are inclined. The most inclined rings, 6, 5, and 4, achieve maximum heights above Uranus' equatorial plane of 24 to 46 km. These three rings are also among the narrowest; their modeled mean widths, corrected for the effects of diffraction and finite star diameter, are all 3.5 km or less. The η ring, equally narrow, is accompanied by a shoulder 55 to 60 km wide and of variable optical depth ($\tau \leq 0.1$). The Earth-based data also showed the ϵ ring to be by far the widest and most eccentric of the rings. Its eccentric radial amplitude is 404 km, five times larger than that of the next most eccentric ring (ring 5).

All nine rings vary in width and optical depth with position around the ring; in

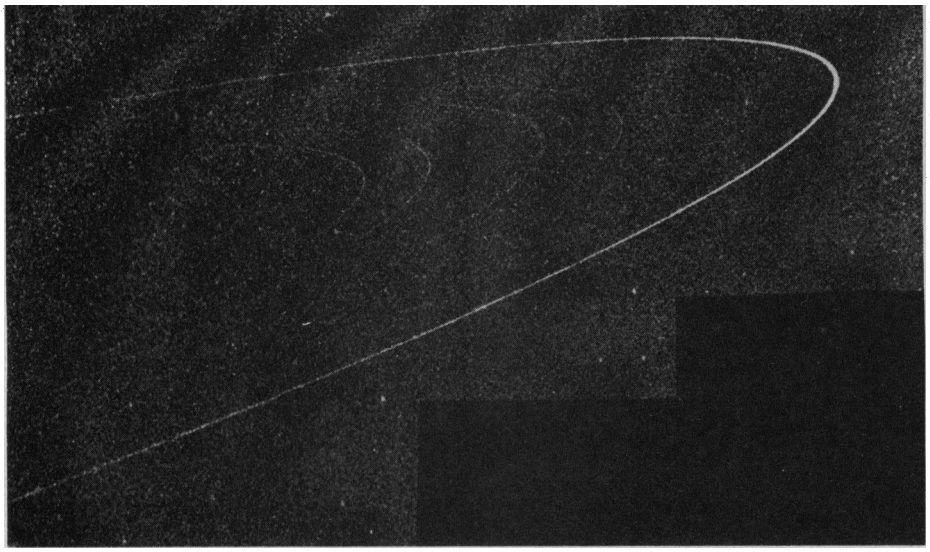

Fig. 10. Three-frame mosaic of the rings near ring plane crossing. Because the slant angle of the rings was changing rapidly during this sequence, all three of these wide-angle images were projected to the same apparent view. The new ring feature 1986U1R can be seen between the outermost ϵ ring (outermost) and the δ ring (the next adjacent bright ring). [Image processing by H. B. de Rueda]

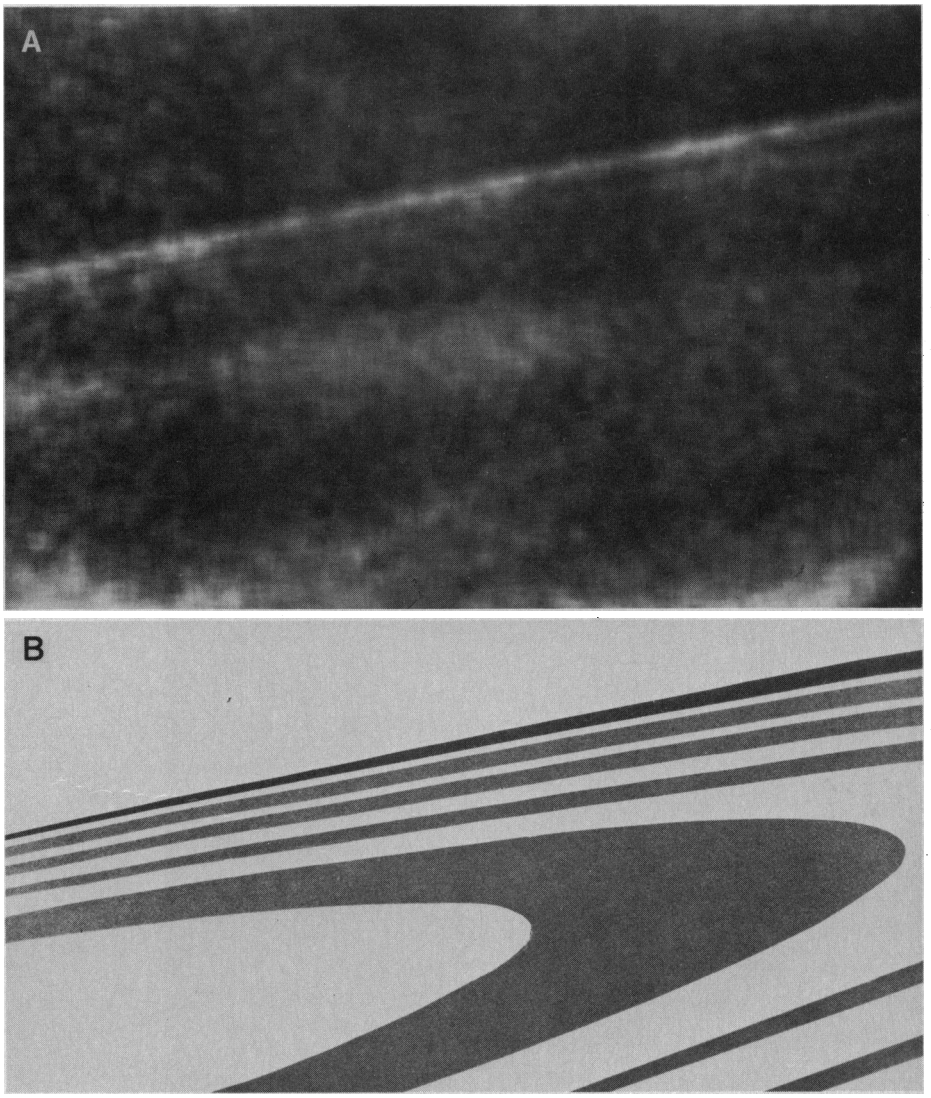

Fig. 11. (A) Enhanced wide-angle image of the region inside the main rings, revealing a broad disk of material. Part of the ring-plane crossing sequence, this image was acquired from a subspacecraft latitude of 4° and a phase angle of 90° and with an exposure time of 7.68 seconds. The image contains about 15 pixels of smear predominantly in the direction perpendicular to the ring plane. (B) Viewing and illumination geometry of this image.

most cases these variations are consistent with a radially integrated mass density independent of azimuth. However, only the widths of the ϵ, α, and β rings vary systematically. The ϵ ring width ranges from 20 km at periapse to 96 km at apoapse. The α and β ring widths range from approximately 5 to 12 km; these extremes occur about 30° from the periapse and apoapse, respectively (*18, 19*).

Earth-based imaging observations of the Uranian rings at 2.2 μm (*20*) and at visual wavelengths (*21*) yield, for both spectral regions, a reflectivity integrated over the entire known ring system of only 1.6 to 2.0%. In actuality, these observations are mostly of the ϵ ring, because it alone contains 70% of the surface area of the rings. Such imaging observations place an upper limit on the optical depth of 0.0015 at 2.2 μm for any diffuse material that is uniformly distributed over the 9300-km extent of the ring system; the upper limit on the product of width and optical depth for narrow rings, observed from Earth-based stellar occultations, is approximately 0.2 km (*18, 19*).

The primary objectives for imaging of the Uranian rings were (i) to observe ring phenomena on azimuthal scales smaller than what could be observed from Earth; (ii) to search for additional rings, both diffuse and narrow, within and surrounding the known rings; (iii) to obtain information about the particle size distribution by observing over a range of phase angles (approximately 12° to 172°) much wider than that observable from Earth (about 0° to 3°); (iv) to determine the reflectivity and color of each ring; and (v) to search for new satellites—those within the rings that might be responsible for ring confinement and those between the rings and Miranda that might play a part in affecting the rings' kinematic behavior.

Inbound, low phase angle observations. Voyager observations during the few days before encounter were made at phase angles ranging from 14° to 25° and at image resolutions of 20 km per line pair or more. Substantial improvements in the stability of the spacecraft since the Saturn encounter made it possible to obtain several unsmeared images of the rings with exposures as long as 15.4 seconds. Two such low phase angle images of the ring system are combined as a mosaic in Fig. 9A. Targeted to capture the ϵ ring at its widest point, this image resolves the ring into two bright inner and outer regions separated by an area of intermediate surface brightness, features observed previously in Earth-based stellar occultations. Except for the ϵ ring (Fig. 9B) and the broad outer shoulder of the η ring (Fig. 9C), all rings were unresolved in even the best unsmeared low phase angle frames. From occultation modeling of the ring shapes, the α and β rings are predicted to be 10 and 12 km wide, respectively. Although Voyager images show systematic azimuthal variations in total integrated brightness around the α and β rings, and although frames such as those in Fig. 9A contain evidence for small-scale azimuthal variations in the brightnesses of the remaining rings (including the broad component of η) more detailed analyses and modeling are required to obtain information about longitudinal variations in the surface brightness of the rings.

For the resolved rings, the ring particle

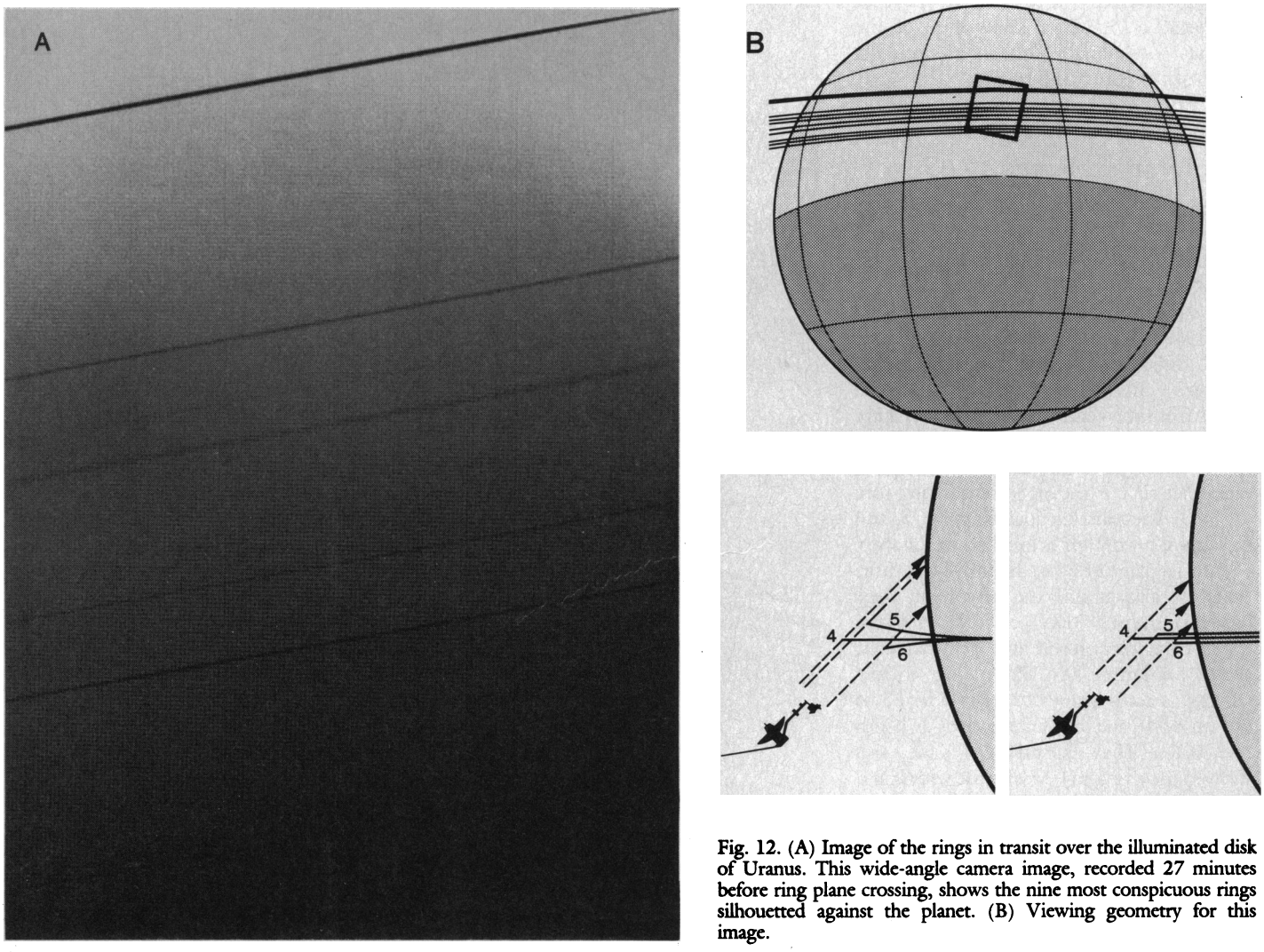

Fig. 12. (A) Image of the rings in transit over the illuminated disk of Uranus. This wide-angle camera image, recorded 27 minutes before ring plane crossing, shows the nine most conspicuous rings silhouetted against the planet. (B) Viewing geometry for this image.

albedo may be determined once the optical depth, or fractional cross-sectional area of the particles, is known. It has been pointed out recently that these fractional cross sections are about one-half the generally accepted values derived from Earth-based stellar occultations, indicating a particle surface albedo of 0.04 to 0.05 at visual wavelengths (*22*). Initial analysis of Voyager images of the ϵ periapse and apoapse points has given comparable low albedo values, assuming periapse to be opaque and angular variation of particle albedo to be zero. Similarly, low particle albedos are inferred for the resolved, low optical depth component of the η ring. These estimates of a few percent for the geometric albedo of the particles should be improved as more accurate calibrations of the imaging data and direct measurements of the ring optical depths from the Voyager stellar and radio occultation experiments become available.

To gain further information about the optical properties of the rings, several color sequences were acquired. Because of the very low ring surface brightness, the smear characteristics, and the low throughput of the color filters, the average signal level in these color images was less than 1 DN for all but the ϵ ring. (A DN, or data number, is the smallest unit of digitized image brightness.) Brightness values were averaged along each ring over as large an azimuthal extent as possible to increase the signal-to-noise ratio. We averaged the results for two sets each of green, violet, and clear images. The reflectivity at the apoapse of the ϵ ring, which is the only resolved ring, is identical in all filters to within the measurement uncertainty (~10%). We conclude that the ϵ ring is gray. Absolute reflectivities of the remaining rings could not be measured reliably in these frames. When scaled relative to the ϵ ring, apparent differences in color were initially seen; however, the total integrated light from each ring differed between filters by less than twice the estimated uncertainties. Thus, a more careful analysis will be needed to determine whether any color variations exist.

Figure 9A also shows a narrow-angle image acquired from 1.12×10^6 km (resolution ~ 20 km per line pair) that contains the first Uranian ring discovered by Voyager. The ring, designated 1986U1R, has a typical reflectivity (*23*) of only about 10^{-4}. At the level of the noise, hints of radial structure can be seen. This and five subsequent views of the ring (including those in Figs. 10 and 13) were acquired at different azimuths and are consistent with a circular ring of orbital radius 50,040 ± 15 km [in a system defined by the absolute radii assigned to the known rings (*19*)]. Another previously unknown ring was detected in backscatter outside the β ring. This feature, whose brightness is roughly one-tenth that of the β ring, is faint in the three images in which it is seen and is situated at an orbital radius of about 45,736 km. No evidence of eccentricity has been found. Searches for other features in inbound images have not yielded credible positive results, even though extremely faint features at or below the noise level are suggested in some images.

Ring plane crossing: Intermediate phase angle observations. Figure 10 is a mosaic of three in a series of four images taken from a distance of 1.18×10^5 km and a subspacecraft latitude of approximately −5° about 11 minutes before Voyager crossed the ring plane. All nine previously known rings are visible, as is 1986U1R. The innermost image of this series (Fig. 11A) reveals a broad band of material inside ring 6 never reported in Earth-based observations. The significant differential smear in this frame is due to the relative motion of the spacecraft and the rings. The exposure time of this image was 7.68 seconds, resulting in about 15 pixels of smear on the far arm of the rings and significantly more on the near arm. Nonetheless, because the smear is dominantly in the direction perpendicular to the ring plane, the natural radial width of any feature in this geometry is preserved at the ring ansa. Measured at this location in the image, the broad sheet of material covers a radial range of 37,000 to at least 39,500 km; the uncertainty in these numbers is approximately 200 km. Radial structure may be present in this feature, but further inspection is necessary to confirm it. This diffuse inner ring has an *I/F* value (*2*) in the range of 10^{-4} in this image, which was taken at an inclination angle of less than 5° (Fig. 11B). For phase angles of about 90°, the reflectivity of a particle (*23*) is probably on the order of 10^{-2} whether the particle is microscopic or macroscopic; therefore, the optical depth of the diffuse sheet is probably in the vicinity of 10^{-3}. However, without further knowledge of the particle size, we cannot even begin to estimate the mass of this feature.

A view of the rings silhouetted against the planet, taken with the wide-angle camera from a ring-plane elevation angle of 9.8° about 30 minutes before closest approach, is shown in Fig. 12A. The spacings of the 6, 5, and 4 rings are markedly different in this image than in the basically pole-on view of the inbound images (Fig. 9). This is a direct consequence of the inclinations of the rings and the position of the spacecraft with respect to the nodal lines of rings 5 and 6, which differed at the time of encounter by 160°. The configuration of the rings in this geometry (Fig. 12B) matches predictions for ring positions from Earth-based models (*19*). Any discrepancies in the match are

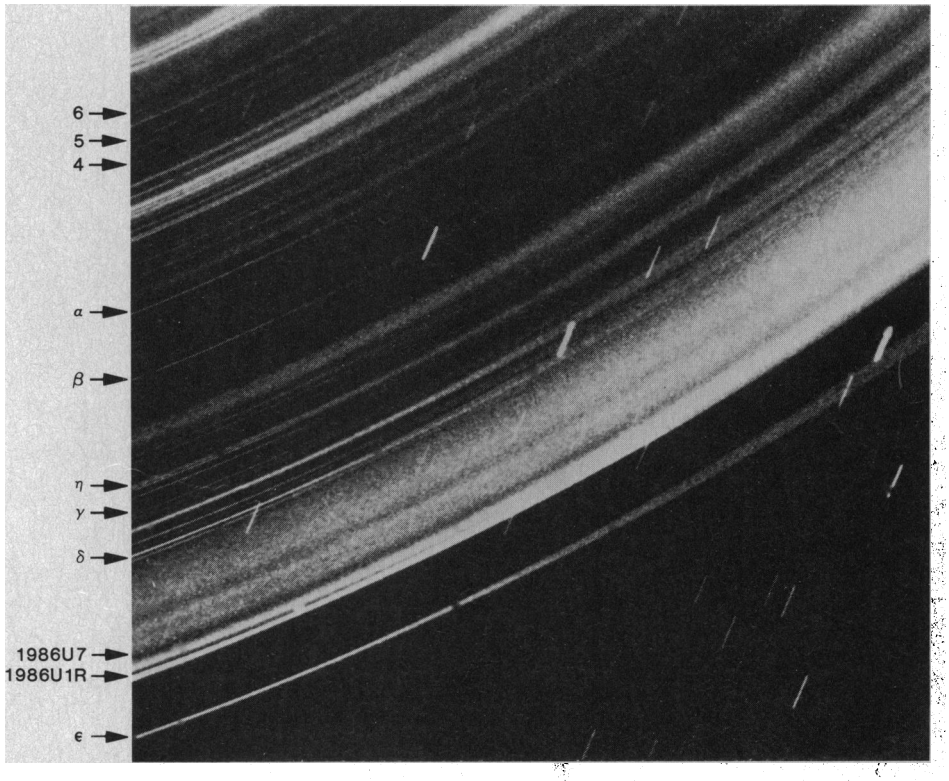

Fig. 13. View of the ring system at high phase angle (172.5°). This 96-second wide-angle image was taken while the spacecraft was in the shadow of Uranus. The high phase dramatically enhances the visibility of the micrometer-sized dust particles. The positions of the known ring features are indicated on the side.

comparable to the uncertainties in the inclinations assigned in those models. Consequently, although a view from low spacecraft latitude provides a far better geometry from which to measure and refine inclination than does the pole-on geometry of Earth-based observations made during the past 10 years, we do not expect that Earth-based values of inclination can be improved by Voyager imaging results alone.

The γ and 5 rings in Fig. 12A are significantly less conspicuous relative to other rings than in, for example, Fig. 9. This difference may be due merely to different combinations of width and optical depth between the rings at the longitude of the image (Fig. 12B). Specifically, the PPS observations (*24*) show that the γ ring is far narrower and more opaque than its neighbors; that it is completely unresolved readily explains the appearance of Fig. 12A.

High phase angle observations. After Voyager emerged on the antisunward side of the rings, a sequence of images was acquired to take advantage of the forward-scattering brightness-enhancement of the micrometer-size particles that have been seen in the Jovian and Saturnian ring systems. The image in Fig. 13 was taken through the clear filter of the wide-angle camera at a phase angle of 172.5° and a range of 2.25×10^5 km from the region of the rings shown. The planet was then occulting both Earth and the sun as seen from Voyager; the lack of scattered sunlight provided the opportunity to obtain this long-exposure (96-second) image to search for extremely low optical depth material. The image was targeted at the location on the rings where the component of the spacecraft smear in the radial direction vanished. The combination of orbital and spacecraft motions in the azimuthal direction amounted to 1400 km in 96 seconds, smearing out azimuthal variations below this scale. The differential radial smear in the rings from left to right across the frame results from the curvature of the rings. In spite of the large azimuthal smear, a suggestion of azimuthal structure can be seen in the frame.

Using the best current model (*19*) for the nine known rings, the spacecraft trajectory data, and the predicted camera direction, we computed the predicted locations of the rings in the frame. Once the locations for the α and β rings are aligned with the bright features in Fig. 13, the remaining rings fall at the indicated positions. All nine main rings are identifiable in the image; although the narrow component of the η ring is not seen as a bright feature, its broad component is easily visible. The closest point to Uranus on the ring plane in this image is about 39,800 km, roughly the same as the outer radius of the broad sheet of material detected at ring plane crossing (Fig. 10). The brightest feature in Fig. 13 falls at the position of 1986U1R, the newly discovered tenth ring. The feature is 38 km wide and is bounded on either side by sharp edges. Structure in the vicinity of 1986U1R may be associated with structure seen faintly in backscatter. Just inward of 1986U1R is a dark but not completely empty lane coinciding approximately with the orbit of 1986U7. The structure of this lane has

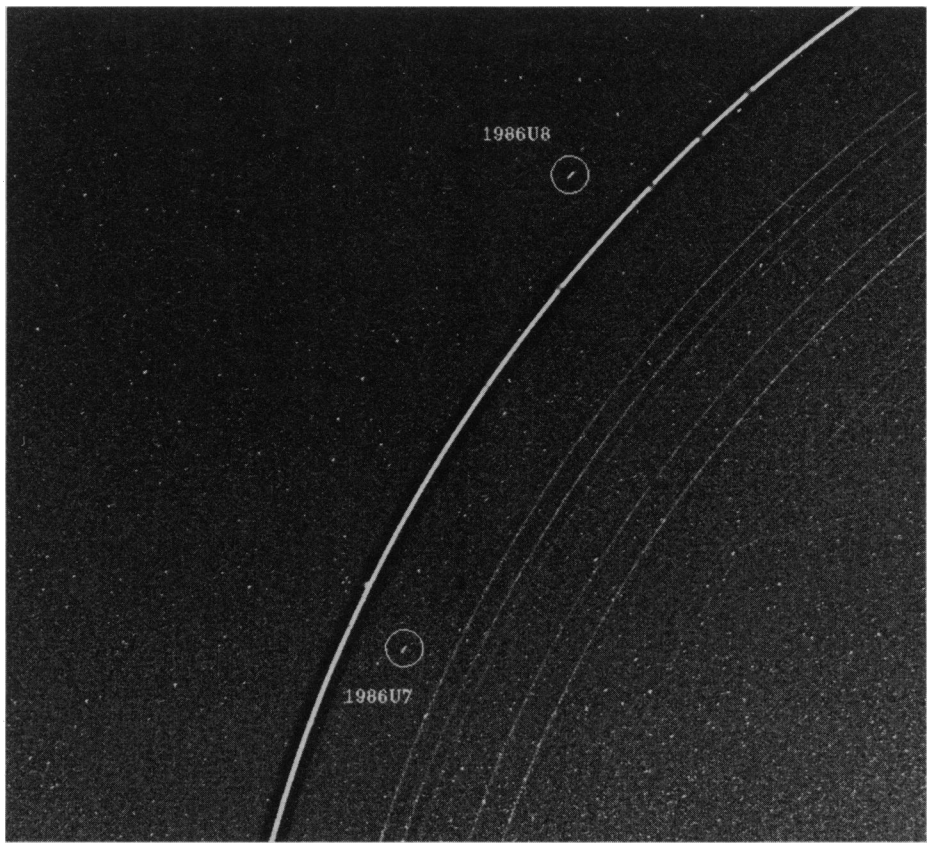

Fig. 14. Shepherd satellites in the Uranian rings. The two satellites designated 1986U7 and 1986U8 are on either side of the ε ring. Resonances from these satellites are near the ε ring edges and may be responsible for confining the ring.

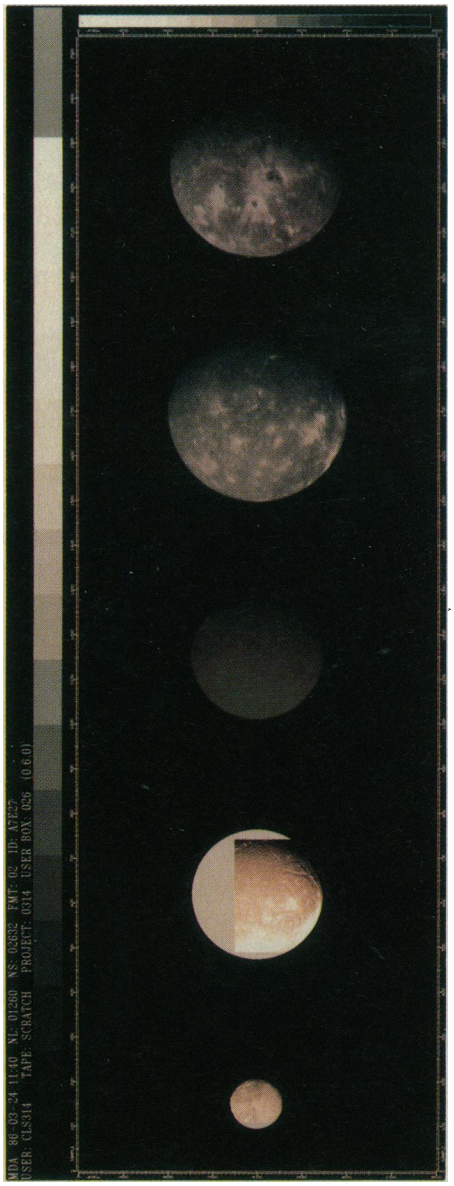

Fig. 15. Montage of Uranus' five largest satellites. From top to bottom in order of decreasing distance from Uranus are Oberon, Titania, Umbriel, Ariel, and Miranda. Images are presented to show correct relative sizes and brightness. Coverage is incomplete for Miranda and Ariel; gray circles depict missing areas. [Image processing by C. L. Stanley]

important implications for the behavior of small particles under the simultaneous disturbing influences of a shepherding satellite, gas drag, and plasma drag; all such forces may affect small particles in orbit around a planet that has a displaced and highly inclined magnetic field and extended exosphere (*25–27*).

The amount of detail in this frame and its spatial scale is perhaps the most unusual result of Voyager's ring observations at Uranus. Features as narrow as the resolution limit (12 km per pixel) are visible. However, with the exception of the nine previously known rings, the two new ones discovered by Voyager in backscattered light, and the features outside the β ring, none of the remaining bright narrow features in this frame can be seen in backscattered light. Moreover, the brightness of this region is low; the apparent reflectivity, *I/F* (*2*), is typically 10^{-4}, with the brighter regions typically 10^{-3}. These brightnesses are far too high to be produced by rings of macroscopic particles that would not have been detected either by Earth-based stellar occultation or direct reflectivity observations or by inbound Voyager imaging observations. Rather, the brightness requires the strong forward-scattering characteristic of wavelength-sized "dust" particles such as that observed in the Jovian ring and in various regions of Saturn's rings. This obvious lack of correlation between regions of high dust density and of large particles is discussed below.

Searches for small satellites. The Voyager 2 cameras were used to search for satellites not observable from Earth that might be associated with the ring system. It had been suggested that the nine extremely narrow rings might be confined by pairs of small satellites (*28*) that apply torques to the ring particles to counteract their natural spreading tendency. Imaging sequences were planned to search the areas between Miranda and the ε ring as well as within the ring system.

The images revealed ten new satellites, one orbiting just inside the ε ring and the remaining nine orbiting outside the rings and inside the orbit of Miranda (Table 2). The largest, outermost, and first discovered, 1985U1, orbits about halfway between the ε ring and Miranda. Except for 1985U1, most of these objects are only a few pixels wide in the images. Estimating albedos and diameters is difficult at such low resolutions; the values given Table 2 represent minima for albedo and maxima for diameters.

The ten small satellites lie in a series of concentric, nearly circular orbits, roughly coplanar with Uranus' equatorial plane. Figure 14 shows two of the new satellites, designated 1986U7 and 1986U8, straddling the ε ring in an image taken from a range of 4.1×10^6 km. The nine smallest satellites all appear to have reflectivities of a few percent, comparable to the reflectivities of the ring particles and 1985U1.

Table 2. Satellite properties. Orbital data for the five large satellites from Veillet (*39*). The visual geometric albedo, P_v, was calculated from Earth-based observations using the new radii for the satellites.

Object	Semimajor axis (km)	Radius (km)	Density (g cm^{-3})	Estimated normal albedo*
1986U7	49,700 ± 50	~20		<0.10
1986U8	53,800 ± 50	~25		<0.10
1986U9	59,200 ± 50	~25		<0.10
1986U3	61,800 ± 50	~30		<0.10
1986U6	62,700 ± 50	~30		<0.10
1986U2	64,600 ± 50	~40		<0.10
1986U1	66,100 ± 50	~40		<0.10
1986U4	69,900 ± 50	~30		<0.10
1986U5	75,300 ± 50	~30		<0.10
1985U1	86,000 ± 50	85 ± 5		0.07 ± 0.02
Miranda	129,783 ± 66	242 ± 5	1.26 ± 0.39	0.34 ± 0.02
Ariel	191,239 ± 57	580 ± 5	1.65 ± 0.30	0.40 ± 0.02
Umbriel	265,969 ± 48	595 ± 10	1.44 ± 0.28	0.19 ± 0.01
Titania	435,844 ± 86	805 ± 5	1.59 ± 0.09	0.28 ± 0.02
Oberon	582,596 ± 71	775 ± 10	1.50 ± 0.10	0.24 ± 0.01

*Estimated from a phase curve for Titania that includes the opposition surge.

Although there appears to be a weak clustering of semimajor axes between 58,000 and 70,000 km, the small satellites (excluding the two ring shepherds) are distributed roughly uniformly between the rings and 1985U1. This distribution is different from that of Saturn's small satellites, which include three Lagrangian satellites (Tethys and Dione), two coorbitals, and three ring shepherds. Another major difference between the small satellites of Uranus and of Saturn is that the Uranian bodies are all dark, whereas the Saturnian bodies are all bright. This may suggest significant differences in formation conditions, in subsequent evolution, or in processes operating on the small Uranian satellites compared to their Saturnian counterparts.

Bounds on undetected satellites in the rings. Several imaging sequences were scheduled in the last 3 days of Voyager's approach to search for satellites embedded in the ring system. The most useful sequence consists of 150 narrow-angle frames shuttered virtually continuously over a 13.5-hour period beginning about 3 days 5.5 hours before closest approach; the range to the planet during the sequence was 4.2×10^6 to 3.5×10^6 km. These images were targeted at a fixed nonrotating position on the rings so that all ring material and embedded satellites would be covered in the sequence. The 13.5-hour period of observation spanned about 2.2 orbital periods of material at ring 6 (radius ~42,000 km) and about 1.6 orbital periods of the ε ring. In addition, because the orbital velocity of material in the 6 ring is about 12 km sec^{-1}, even the fastest ring object would take 30 to 35 minutes to cross the narrow-angle field of view. Because the frames were shuttered approximately every 6 minutes, an object should be observable in at least four or, more likely, five or six frames, making possible the confirmation or rejection of the identification of new satellites.

Subsequent spot coverage with the narrow-angle camera imaged approximately 80 percent of the orbital longitudes of the rings. Although shuttered to within 1 day and 10^6 km of closest approach, this sequence has insufficient redundant narrow-angle coverage; thus we could not confirm or reject suspect identifications. Predictions of the location of candidates in earlier narrow-angle frames will eventually provide a means of their confirmation or rejection. For this initial report, we therefore establish a bound on the size of undetected satellites on the basis of the earlier 150-frame sequence. By comparison with the resolved image of the inner ε shepherd 1986U7, the radius of the outer shepherd 1986U8 is estimated to be 25 km (Table 2). The outer shepherd was observed to be about 8 DN above background in a 15.36-second, narrow-angle, clear-filter frame taken at about 3.6×10^6 km during the 150-frame sequence. The shepherd's image was actually a streak 8 pixels long, and therefore the effective exposure was only 2 seconds. Orbital motion alone accounted for about 5 pixels of the streak's length. Therefore, an integration time of only 2 or 3 seconds will occur in most cases (except for those in which other random motions significantly add to or cancel the smear). A 2-DN, 8-pixel streak in such a frame would also be easily visible; therefore, an object about 15 km in radius would be detectable unless its apparent re-

flectivity was considerably lower than those of the known shepherds (about 2% at these phase angles). Because a 1-DN, 8-pixel streak would also be visible, redundant frames may allow the detection limit to be lowered to a radius of about 10 km (reduced by $\sqrt{2}$). We therefore adopt a current detection limit of a 10-km radius for the entire region of the main rings. We expect that careful analysis of the nonredundant spot coverage will eventually allow reduction of this diameter limit by about a factor of 2.

Discussion of the ring observations. The ring systems of the outer planets differ considerably in particle properties, overall optical depth, and radial structure. The Voyager data have shown that the particle albedos in at least the ϵ and η rings are low (about 5%), comparable to the low albedos of the newly discovered small satellites associated with the rings. These direct results are in good agreement with estimates made of ring material albedo using Earth-based observations before Voyager data were obtained (*21*, *22*). Initial analyses of the relative brightnesses of the other rings suggest similarly low particle albedos. The dark, colorless surfaces of the Uranian ring particles are important in the study of the origin and evolution of the ring-satellite system; they contrast sharply with the brighter and definitely reddish surfaces of the ring particles and satellites of Jupiter and Saturn. The nine main Uranian rings, although similar in kinematics and structure to the narrow ringlets observed in Saturn's rings (*29*), are also unusual in that their fractional abundance of dust is low. From high phase angle Voyager images we estimate the areal fraction of micrometer-sized particles in the main rings to be of order 10^{-3} to 10^{-4}. For comparison, optically thick parts of Saturn's rings contain several percent dust (*30*), and Jupiter's ring is thought to have roughly comparable optical depths due to dust and macroscopic particles (*31*).

The presence of micrometer-sized dust particles is of interest primarily because such small particles are short lived in any ring environment. Thus their presence indicates local sources—for example, larger particles that can survive the processes of drag, sweepup, and erosion that can rapidly remove micrometer-sized particles. Contrary to our suspicions at the time of encounter, closer investigation of the magnetic field perturbations shows them to be of questionable importance (*32*). However, the results of the Voyager UVS investigation at Uranus (*6*) indicate that, at the η ring for example, the extended Uranian exosphere and (extrapolated) neutral atom densities are high enough to remove a 1-μm particle in about 2000 years by gas drag alone (*26*). This rate is equivalent to the removal of several 10-m radius objects per year or of one 25-km radius object in the age of the solar system. Thus the dust may well be in steady state, being regenerated by some process at the same rate at which it is lost from the system by gas drag. Because of the rapid orbital decay of micrometer-sized particles, no shepherding process would be effective on the inferred dust shown in Fig. 13.

Possible sources of dust in moderately opaque rings include locally active, internal processes such as collisions caused by spiral-wave damping or shepherding by nearby small satellites (*30*). Another such process may be collisions among parent bodies that are more energetic in the optically thin inter-ring regions and that thereby liberate more dust upon collision.

Alternatively, the creation of dust may result from the direct impact of meteoroids onto as yet unseen parent bodies only a few kilometers across [as is likely for the Jovian ring (*31*)] or onto debris belts maintained by such parent bodies in "horseshoe orbits" (*33*), thereby preventing rapid orbital decay caused by gas drag. The low optical depth of such belts of parent macroscopic particles would be more easily maintained in horseshoe orbits than by gravitational torques, whose operation requires collisional damping. Even such bands of macroscopic debris as may currently exist may themselves be only transient products of recent large meteoroid impacts. In this "external production" scenario, the lack of correlation of the brightest dusty features with the main rings of high optical depth (Fig. 13) would require the mechanism that removes the dust to be more efficient in the main rings than elsewhere.

The dust in the rings (Fig. 13) exhibits considerably more fine structure and an optical depth that is orders of magnitude higher than the dust in the Jovian ring and in Saturn's G and E rings. The Uranian dust rings are similar in structure to the D ring of Saturn. Both Saturn's D and the Uranian rings contain multiple, narrow, well-defined bands of material of low optical depth with no obvious dynamical means of maintenance. Like Saturn's D ring (*34*), the brightness of the dusty features in the Uranian rings, as seen in forward scattering, correlates poorly with the optical depth of the underlying larger particle material (*34*).

Regardless of the process responsible for the optically thin dusty bands, the nine main rings require some active shepherding process that will function in the presence of the inevitable energy loss that accompanies their frequent interparticle collisions; evidently they require some form of gravitational torque. A major contender for the role of maintaining narrow, high optical depth rings has been the shepherding mechanism proposed by Goldreich and Tremaine (*28*) after the discovery in 1977 of the narrow, opaque Uranian rings. The process involves excitation and damping of orbital eccentricities in ring material by nearby satellites; the net result is a transfer of angular momentum that keeps the ring material away from the satellites.

There are several manifestations of the shepherding process that involve similar physics but produce quite different results. One of the most important factors is whether the perturbing satellite is close enough to its "flock" for overlap of multiple Lindblad resonances (*35*). This is the case for Saturn's Encke gap, which is cleared by an embedded shepherd (*36*). However, when the satellites become so far from the ring that the distance between successive Lindblad resonances becomes larger than the interaction width of the resonances, the ring edges may be maintained by discrete inner and outer Lindblad resonances with the shepherding satellites (*37*). This process is much more likely to take place in the Uranian ring environment than at Saturn because the Uranian rings are several times closer to their parent planet; the correspondingly larger gradient of angular velocity leads to lower wavenumber (more widely spaced) resonances for a given ring-satellite separation. In this case, a satellite could only control the ring's edge in the same manner that Mimas controls the outer edge of Saturn's B ring (*38*).

We searched for Lindblad resonances of the outer and inner ϵ shepherds that fall near the ϵ ring. These locations were computed from the mean motions determined from multiple imaging observations of each satellite. The spacing of the inner Lindblad resonances of 1986U8 is approximately 200 km at the ϵ ring; the spacing of the outer Lindblad resonances of 1986U7 are about 60 km at the ring—much greater than either the resonance width $[(M/M_U)^{0.5}]R$ (where M is the ring mass, M_U is the mass of Uranus, and R is the distance between Uranus center and the ring) (*35*) or the ring's width. Thus, the resonances seem to be nonoverlapping. A more complete understanding of the relation of such resonances to ring edges must await the refinement of the ring radii from Voyager tracking data and of satellite orbital elements. However, as judged from current values, it does appear that high wavenumber inner and outer Lindblad resonances lie at the outer and inner edges of the ϵ ring, respectively, to within the uncertainties; they may therefore be responsible for this ring's confinement.

We are still left with the problem of the confinement mechanism of the eight inner

main rings. Analyses of the irregularities in their radii, widths, and precession rates, as determined from Earth-based stellar occultations, have established limits on shepherding satellite radii of about 10 km (*19*); this limit is comparable with results presented here based on our best fully redundant coverage.

The Satellites of Uranus

Studies of the Uranian satellites before the Voyager 2 encounter were limited to dynamical analyses and disk-integrated photometry, radiometry, and spectroscopy. The orbits of the five largest Uranian satellites (Miranda, Ariel, Umbriel, Titania, and Oberon) are all of low inclination [except that of Miranda (inclination ~4°)] and low eccentricity. The orbital dynamics (*39*) and physical properties (*40*) and a new analysis of the possible tidal evolution (*41*) of the Uranian satellites have been reviewed recently. Most models require that the satellites formed in orbit after the inferred early cataclysm that produced Uranus' large obliquity. All the satellites were expected on theoretical grounds to be in synchronous rotation, keeping the same side toward Uranus (*42*); Voyager images show that the rotation periods of the five largest satellites are synchronous to first order.

Analysis of infrared radiometry and spectral reflectance (*43, 44*) provided the first reliable estimates of the radii of the five largest Uranian satellites; these values have been confirmed by the significantly more accurate Voyager 2 imaging observations. Analysis of telescopically acquired reflectance spectroscopy (*43, 45*) indicated the presence of water ice on all of the five largest satellites, but radiometric observations (*44, 46*) suggested that Umbriel, Titania, and Oberon have lower albedos than would surfaces of pure water ice that were heavily "gardened" by meteoritic infall. More detailed spectral observations suggested that the surfaces of Ariel, Umbriel, Titania, and Oberon were covered partly by dark, spectrally neutral material (similar to charcoal, carbon black, or carbonaceous chondritic material) and partly by bright water frost in varied proportions (*47, 48*).

Caution must be exercised in interpreting the Voyager observations of the satellites as representative of their entire surfaces. Because the subsolar points on Uranus and its satellites are currently close to their south poles, Voyager images (such as those shown in Fig. 15) cover only the southern hemispheres. Also, the terrain types of many objects in the solar system display global dichotomies (for example, the southern highlands and the northern lowlands of Mars and the dark leading and bright trailing hemispheres of Iapetus).

Bulk properties. The satellites of the Uranus system range in size from the relatively small inner satellites discovered by Voyager 2 to the two largest outer satellites, Titania and Oberon (Table 2). Mean density is an important constraint on the bulk composition of a planetary body. Mass determinations are generally difficult to make, requiring either measurement of acceleration of a spacecraft during a flyby (from Doppler shifts in the frequency of the spacecraft radio transmitter) or complex numerical solutions of the orbital motions; Earth-based observations alone have not produced accurate mass estimates (*58*). Voyager 2 passed close enough only to Miranda for a Doppler mass determination (*5*). The masses of Ariel, Umbriel, Titania, and Oberon were determined by fitting the optical navigation position measurements of these satellites with a numerically integrated model of their motions; the residuals in the fit were about 0.2 pixel. About 70 orbital positions each for Miranda, Ariel, and Umbriel and about 40 each for Oberon and Titania were acquired with the narrow-angle camera from early November 1985 through late January 1986 at ranges from about 10^8 km to about 10^6 km. Thus, position-measurement accuracies ranged from a few to a few hundred kilometers. Relatively short-period (145-day), large-amplitude (800-km) variations in the motions of Titania and Oberon dominate the optical sensitivity to the masses of these two satellites (*49*); similar terms in the motions of Ariel and Umbriel have not yet been identified from theoretical considerations.

The current best estimates of the satellites' masses, radii, and equivalent densities are shown in Table 2 and plotted in Fig. 16. The masses are averages of a series of numerical least-squares experiments that used a combination of the Voyager Doppler and optical measurements described above coupled with Earth-based astrometric measurements made over about 6 years. The error bar for Miranda's mass is limited by the Doppler data; the uncertainties for the other four satellites are mostly dependent on the optical navigation data. Inclusion of the radio tracking data (*5*) reduces the errors for Ariel, Umbriel, and Titania by about 25%, but it does not reduce the error for Oberon.

Phase behavior. Earth-based measurements in the visible and near infrared wavelengths show that the brightnesses of Ariel, Titania, and Oberon increase rapidly with decreasing phase angle at angles less than about 3° (*47, 50*). Voyager 2 was able to acquire low phase angle images of Titania (Fig. 17). Inside a phase angle of 3° the data are consistent with Earth-based observations of the full-disk opposition surge. The lowest phase angles reached for the other satellites were 10° to 13°. High phase angle data (139° to 153°) were acquired for Ariel, Umbriel, Titania, and Oberon. The disk-integrated phase curves of the satellites are

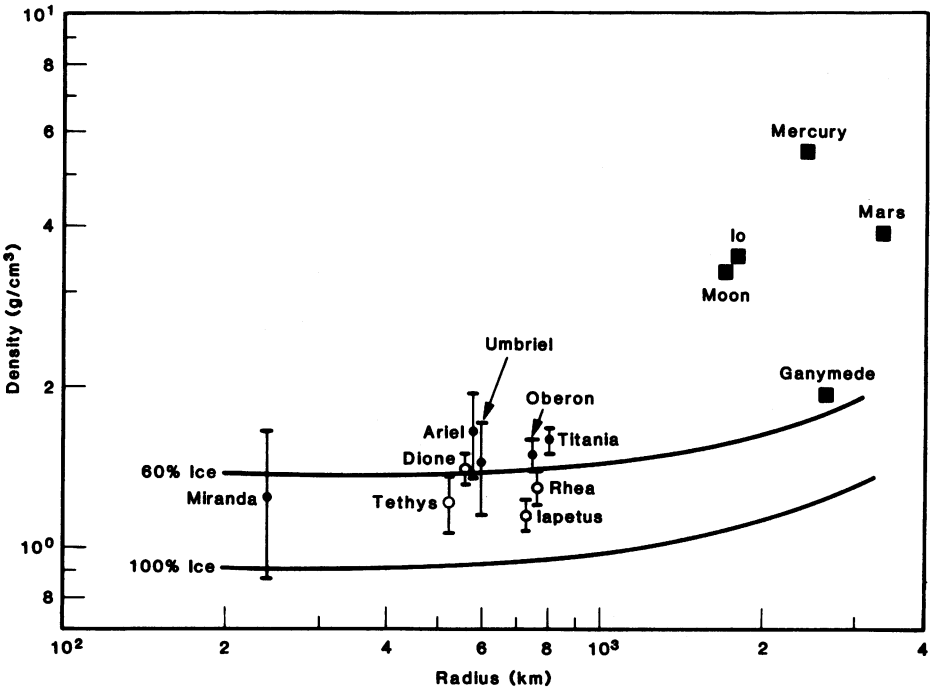

Fig. 16. Density plotted against radius for several satellites with other objects for comparison. The solid lines are models for objects consisting of pure water ice and a mixture of 60% water and 40% silicate, illustrating the effects of self-compression modeled by Lupo and Lewis (*66*).

similar in the region of overlapping coverage (Fig. 17).

The Voyager observations of Titania's phase curve can be fitted well by using the photometric theory of Hapke (*51*). The results indicate a compaction parameter of 0.02; the value derived for Earth's moon is 0.05 (*51*). The lower value for Titania suggests that its surface layer is even more porous than that of Earth's moon. Another important indication of the fit is that the large-scale roughness of Titania is similar to that of the moon. Thus the Hapke theory fits the data well; the exotic particle properties that have been proposed (*52*) are not required.

Albedo and color. The disk-integrated normal reflectances of the individual satellites (Table 2) is estimated from clear-filter images of the whole disk and application of a phase correction derived from analysis of the Titania images. Figure 18 shows no simple trend in albedo with distance from Uranus, although all the objects inside Miranda's orbit appear to be uniformly dark. In addition, the satellites of Uranus are generally much darker than those of Saturn (except for Phoebe and the dark regions of Iapetus).

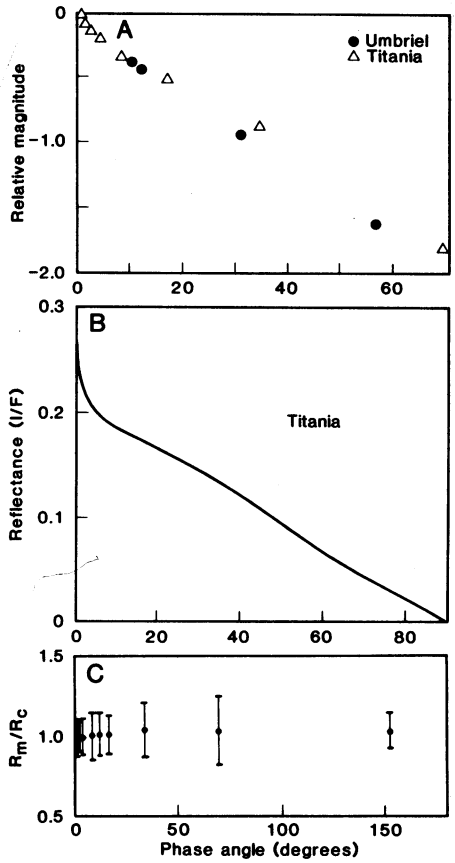

Fig. 17. (A) Disk-averaged phase curves for Titania and Umbriel in relative magnitude as a function of phase angle. (B) Fit of Hapke's new theory (*51*) to the Voyager Titania phase observations. The parameters of the fit are $w = 0.66$, $h = 0.02$, $b = -0.36$, $c = 0.70$, $\bar{\theta} = 28°$, and $S(0°) = 0.86$. (C) Deviation of the model from the observations: R_m, Voyager observed values; R_c, calculated values.

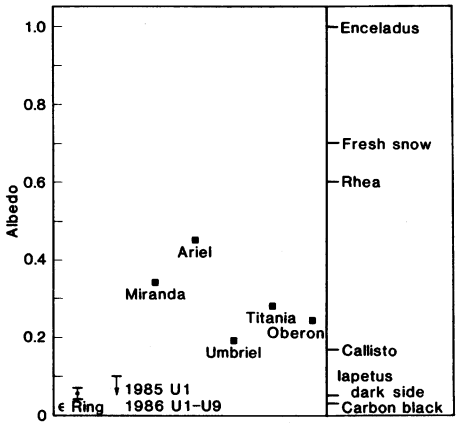

Fig. 18. Albedos in the Uranian system. The geometric albedos of the five largest Uranian satellites are plotted from the Voyager radii. The *I/F* values observed for ε ring particles and 1985U1 through 1986U9. The albedos of some Saturnian and Jovian satellites and of some light and dark materials are shown for comparison.

The disk-averaged albedos at the central wavelengths of the narrow-angle camera filters for Miranda, Ariel, Umbriel, Titania, and Oberon are shown in Fig. 19. The disk-averaged colors are gray. Even Oberon, the reddest, is quite gray; its color is similar to that of Phoebe and many C-type asteroids. None of the satellites is as red as D-type asteroids or Iapetus' dark material. Initial analysis of individual bright and dark areas on the five satellites indicates that all their spectra are quite flat. It is perhaps not surprising that the bright areas have flat spectra because they are probably composed mainly of water ice; the dark material, however, has a surprisingly bland reflectance like that of the dark material in the Uranian ring system. This observation has important ramifications for the origin of Uranian dark material in general.

1985U1. Because 1985U1, the largest of the ten newly discovered satellites, was discovered more than a month before encounter, it was possible to modify the sequence of Voyager activities so that an image of the satellite (Fig. 20) could be obtained. This satellite has a uniform apparent albedo of 0.04 at a phase angle of 33°, corresponding to a geometric albedo of 0.07 (for an asteroidal phase coefficient). With a radius of about 85 km, the object is surprisingly spherical: most objects in the solar system that are of similar size are highly irregular in shape. A few craters are visible on 1985U1, the largest being about 45 km in diameter.

The lack of albedo contrast on 1985U1 and the extremely low albedo of all the newly discovered satellites indicate that their surfaces are unlike those of the large icy satellites of Uranus. Even dark Umbriel is much brighter than these objects. The absence of scars and rays from impact craters on 1985U1 suggests several possible scenarios for its bulk composition. If 1985U1 is predominantly an icy object, composed mostly of water ice perhaps mixed with small amounts of ammonia and methane hydrates, some process must be occurring to erase rapidly any fresh material exposed by impacts on its surface. Possible processes include the continual sweepup of dark material that coorbits with the satellite and some continuous darkening process, such as irradiation of methane or methane clathrate.

Alternatively, 1985U1 may be so uniform internally that crater rays simply never form; that is, it may be composed mostly of rock and dark material or of water ice uniformly mixed with enough dark material to give it its low albedo. In these models, 1985U1 may be a primitive icy or carbonaceous conglomerate that in its present state is representative of the material from which it formed.

Impact populations on the large satellites. The size-frequency distributions of impact craters were analyzed for the entire global coverage of Ariel, Umbriel, Titania, and Oberon and for the most heavily cratered regions of Miranda (Fig. 21). The statistics are complete to diameters of about 3 km on Miranda, 6 km on Ariel, 13 km on Titania, and 25 km on Umbriel and Oberon; the data are limited by resolution at diameters smaller than these.

Oberon and Umbriel display a dense pop-

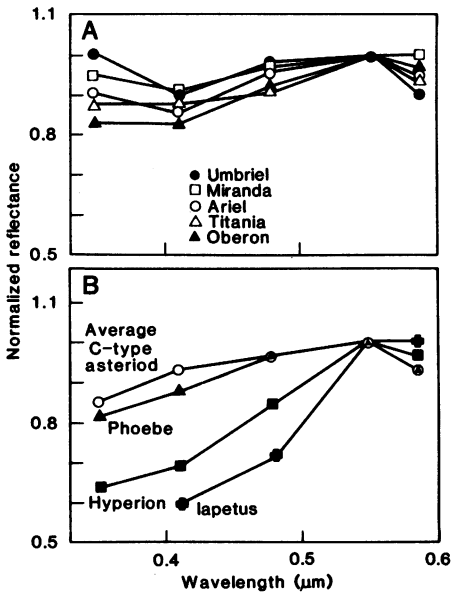

Fig. 19. (A) Disk-averaged colors of the five largest satellites of Uranus. Data are plotted for five filters, scaled to unity at the green filter (0.57 μm). (B) Broadband reflectances at the effective wavelengths of the Voyager filters of an average C-type asteroid, the dark side of Iapetus, and Phoebe.

ulation of large impact craters, especially those between 50 and 100 km in diameter. This population is similar to that of the lunar highlands (Fig. 21) and of many of the most ancient, heavily cratered bodies in the solar system. A similar population was recognized on the oldest parts of the Saturnian satellites (*53*); we refer to this type of crater population as Population I. Such populations are thought to date back to the early sweepup of postaccretional debris that occurred more than 4×10^9 years ago.

In contrast, Titania and Ariel have far fewer craters in the 50- to 100-km size range, but the abundance of smaller craters increases rapidly with decreasing diameter, so that the number (per unit area) of craters about 20 km in diameter on Titania is about the same as the number on Oberon and Earth's moon. The populations on Titania and Ariel have size-frequency distributions resembling those of craters generated by the secondary impact of ejecta from large primary craters. Similar populations were recognized on some of Saturn's satellites, notably Enceladus and Dione (*53*); we refer to this type as Population II.

Miranda's craters are also typical of Population I craters, but the number is greater than on Oberon, Umbriel, and Earth's moon by a factor of almost 3. Because of the small total area of Miranda's cratered terrains, the statistics are weak for diameters larger than about 40 km. The cumulative size-frequency plot (Fig. 21) suggests that some Population II craters are present as well, as indicated by the slight increase in slope at diameters less than about 10 km.

The reasons for the differences in the two populations are uncertain. For the Saturnian system (*53*), we suggest that Population I represents cratering by debris (perhaps remnants from accretion) scattered in heliocentric orbits throughout the very early solar system. Because Titania and Ariel do not show abundant Population I craters, their present surfaces must postdate this period. Again, as for Saturn's satellites (*53*), we suggest that the Population II craters were formed by impact of secondary debris generated by collisions within the satellite system. This debris could have resulted either from large impacts on the satellites or from collisions between other objects, such as Trojan satellites.

Oberon. Voyager 2 observations have confirmed that Oberon (Fig. 22A) and Titania are remarkably similar in diameter, density, color, and albedo, although their cratering records are quite different. A large mountain, perhaps a central peak of an impact structure several hundred kilometers in diameter, protrudes at least 20 km above Oberon's bright limb. What appear to be

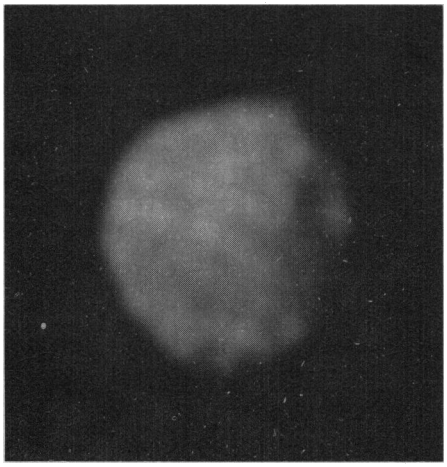

Fig. 20. Image of 1985U1. This is the best image obtained of any of the newly discovered satellites. The resolution is about 9 km per line pair.

linear to curved scarps—probably traces of enormous faults—are faintly visible and are shown on the geologic sketch map (Fig. 22B). They suggest some late-stage, global-scale tectonic episode.

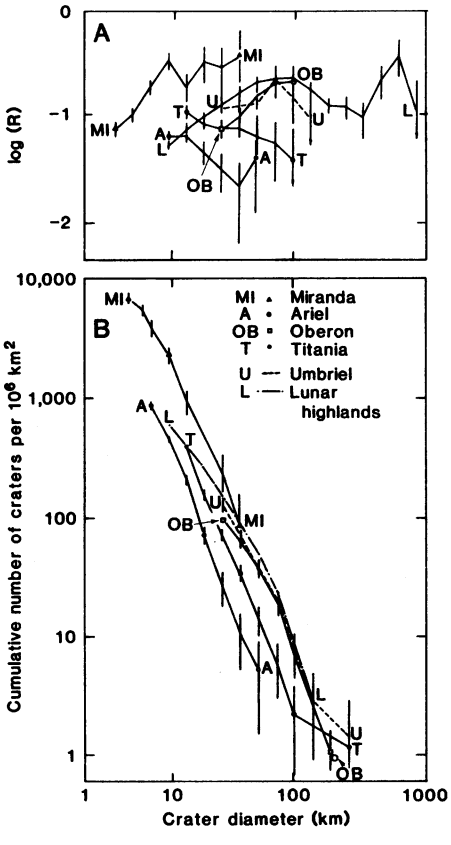

Fig. 21. Crater frequency plot of most densely cratered regions on the five major Uranian satellites and the highlands of Earth's moon. (A) Ratios of each of the crater populations to a standard population as a function of diameter. The standard population is one in which the number of craters larger than a given diameter per unit area is proportional to the inverse square of that diameter. (B) Same data as above, but the number of craters per unit area larger than a given diameter is plotted as a function of that diameter.

Isolated patches of very dark material occur in the floors of a few large craters, some of which are large enough to permit reasonably accurate estimates of their spectral reflectance. These patches have albedos of 0.05 to 0.10, are neutral in color, and may be similar to those in crater floors on the trailing hemisphere of Saturn's satellite Iapetus. The dark material on Oberon's crater floors must have been deposited during the last stages of heavy bombardment, when the large craters formed, or well after it; otherwise, they would have been obliterated by that same bombardment. Perhaps some fluid, either one that was originally dark or one that darkened after surface exposure, was erupted from Oberon's interior. The two most conspicuous deposits of dark material occur in two large craters that have bright rays; they suggest that these late impacts, near the end of heavy bombardment, may have triggered extrusion of dark material. Alternatively, the dark patches could have been deposited long after that period.

Titania. Although similar to Oberon in global properties, Titania is different in appearance when viewed at higher resolution (Fig. 23A). In addition to the abundant Population II craters scattered over the surface, a few large impact basins (100 to 200 km in diameter) are visible. Several patches of smoother material with fewer craters suggest a prolonged early period of resurfacing.

An extensive network of faults cuts the surface of Titania (Fig. 23B). Most faults occur in a branching, partly intersecting network, a pattern commonly observed among normal faults on Earth. Several inward-facing fault scarps bound down-dropped blocks that are almost certainly grabens. As can be seen in the full-disk color image of Titania (Fig. 15), brighter material is exposed along several of these scarps, most notably on a scarp that runs from the terminator across the disk near the subsolar point and continues over the bright terminator. The grabens range in width from about 20 to 50 km; relief of the scarps is about 2 to 5 km (determined by shadow measurements near the terminator). The faulting is indicative of global extension of Titania's crust, which may have occurred in response to the last stages of freezing of ice in the interior of the satellite. The faults cut large craters and do not seem to be strongly modified by the Population II craters. Because only a few craters are superposed on them, the faults are evidently among the youngest geologic features on the satellite.

We propose the following simple sequence for Titania's geologic evolution. Titania once displayed many large (Population I) craters, which were largely obliterated by

extrusion of material onto the surface or by viscous relaxation coupled with continual impact degradation. A few large impacts occurred, due possibly to Population I impactors or debris in orbit with Titania (or both). Subsequent bombardment during this period, however, was dominated by debris generated by objects colliding with Titania or with one another in orbit with Titania. After most of the Population II debris had been swept up, a few regions were resurfaced by another extrusion of material. Finally, the surface of Titania was ruptured by tensional faulting, producing the scarps and grabens. The youngest features on Titania are bright-ray craters whose abundance is roughly what would be expected for impact of comets during the last 3 to 4 billion years.

Umbriel. Umbriel and Ariel have similar diameters and densities, but they differ dramatically in surface properties and in style and degree of geological evolution. As Voyager 2 approached to within a few million kilometers of the Uranian system, it became clear that Umbriel has several enigmatic characteristics. It is much darker than the other four large satellites and displays a weaker water ice spectral signature (*43, 45*). The images reveal a striking uniformity in Umbriel's low albedo. The other large satellites display bright and dark markings whose contrast is typically about 30%. Many of these markings are related to impact ejecta deposits; others are probably due to endogenic processes (such as volcanism or tectonism). In the highest resolution color image (Fig. 15) and to the limits of detection by the Voyager cameras (contrast of a few percent), crater rays did not appear on Umbriel. Only two or three albedo features were detected in the images, the most conspicuous being an annulus of brighter material with an inner radius of about 10 km and an outer radius of about 40 km. Even this bright ring is darker than bright materials that have albedos up to 0.50 on the other large satellites. The early observations suggested that Umbriel's surface might be young, affected by some ongoing process that is erasing impact rays and generating the unusual brighter ring. However, instead of a geologically young surface, a dense population of large Population I craters is shown by the highest resolution view of Umbriel (Fig. 24). The bright ring appears to lie in the floor of one of these large craters. Umbriel's surface appears, along with Oberon's, to be the most ancient of Uranus' major satellites.

How can Umbriel's ancient, cratered topography be consistent with a global albedo pattern that is suggestive of a young, fresh surface? One possibility is that Umbriel, like 1985U1, has been recently coated by a uniform blanket of dark material that has erased previous surface markings. In such a model, the brighter annular ring would have to have been deposited even more recently. This type of model is similar to one proposed for Saturn's satellite Enceladus, which is equally bland but extremely bright. Enceladus orbits near the maximum density of the tenuous E ring; it has been suggested that E-ring material is being swept up by Enceladus, producing a uniform, bright deposit (*54*). This model, if applied to Umbriel, would require a recent supply of dark material orbiting with and being accreted by Umbriel. As proposed for Enceladus, Umbriel would also have to be in some way the source of the material, since neither Titania nor Ariel display evidence of such deposits.

One obvious way in which material could escape Umbriel and enter orbit is by impact. If a large projectile struck Umbriel relatively recently in geologic time, the amount of ejecta generated could easily produce a recognizable coating on its surface; for example, a 10-km crater would produce a 1-cm thick coating. All that would be required is that such a projectile strike relatively dark material and that the material be well mixed in orbit. The problem with this idea is that, for any plausible population of impacting objects, the formation rate of smaller craters (say, 100 m in diameter) would be tens of thousands times higher than the formation rate of the hypothetical 10-km crater. This rain of smaller craters would rapidly destroy a 1-cm-thick layer. Alternatively, the impactor could have been an isolated object, not a member of a large population. This model would require storing a large bolide in orbit about Uranus and bringing it into collision with Umbriel very late in geologic time, which seems to be equally unlikely.

Another way in which material could be ejected into orbit around Umbriel would be explosive eruption. One component that could cause explosive volcanism is methane (*55*). Another possible mechanism is the dissociation of carbon monoxide clathrates, as has been proposed to explain low-temperature degassing of some comets (*56*). Perhaps Umbriel's large, bright annulus is in some way connected to such a phenomenon. A problem with the explosive eruption theory is that such volcanically active processes seem to be inconsistent with Umbriel's ancient surface.

Another possible explanation for Umbriel's dark, uniform character is that the surface material is such that albedo markings generated by crater scars and rays simply never form. This theory requires a material whose optical properties would be unaffected by hypervelocity impact—a characteristic that may be difficult to achieve. This model would also require that Umbriel's subsurface material be extremely uniform to a substantial depth on a global scale. Such uniformity in turn requires (i) that Umbriel was never differentiated but has remained a primitive, cold, uniformly accreted body or (ii) that it developed a deep layer of dark material very early, before the end of heavy bombardment. Such scenarios seem to be inconsistent with the bright ring and other localized bright patches.

Ariel. The surface of Ariel is younger and geologically more complex than that of any of the satellites more distant from Uranus. The oldest geologic feature on Ariel is a widespread cratered unit (Fig. 25, A and B) that displays chiefly Population II craters; the largest of these is about 60 km in diameter. Old, large Population I craters evidently have been lost either by viscous relaxation or by extensive extrusion of material over the surface (or both). The largest remaining crater is flattened and has a gently domed floor partly encompassed by a shallow trough; this configuration has been observed for many craters on the heavily cratered terrain of Ganymede and indicates viscous relaxation of the topography (*57*).

The old cratered unit is broken and offset by a global system of fractures and faults. The freshest and probably youngest of these faults bounds a spectacular system of narrow, deep valleys that can be followed to the limb of the satellite at mid-latitudes in the leading hemisphere. These valleys are almost certainly grabens; the entire fault system probably consists of normal faults developed in response to extension of the crust. Abundant Population II craters have formed on the oldest fault scarps, whereas the youngest fault scarps are nearly free of superposed craters. Evidently the period of faulting and crustal extension spanned the episode of Population II bombardment.

A unit of smooth material occupies the floors of most of the graben valleys in the sub-Uranus hemisphere of Ariel, and it also forms an extensive plain at high latitude near the center of the mosaic (Fig. 25A). This material has clearly been emplaced, at least in part, as a flow or sequence of flows that overlaps and partially buries older craters. Although the crater abundance is lower than on the old cratered unit, Population II craters are superimposed on the smooth material. Hence, the smooth material was emplaced during the episode of Population II bombardment.

Where the smooth material occupies the older fault-bounded valleys, the margins of the smooth unit generally are delineated by troughs. In addition, there are medial grooves or troughs and, in places, medial

ridges on the smooth unit (Fig. 26). The form of the smooth unit, where it is bounded by troughs, suggests that it has been emplaced as highly viscous material—perhaps ice or clathrate at temperatures near the minimum melting temperature—that welled up along the axes of the valleys. Many craters on the smooth material are flattened, probably by viscous relaxation in the relatively warm substrate. The medial grooves may have been formed by renewed faulting or opening of fissures from which the warm ice was extruded; medial ridges may have been formed by late-stage renewed extrusion. The extrusion of viscous material during the time of extensional faulting indicates that the two processes are genetically related. Expansion of the crust during late-stage freezing of the deeper interior of the satellite may have opened the conduits for extrusion of warm, subcrustal material.

The youngest features on Ariel are the bright-rimmed craters and bright deposits; these are probably the ejecta of unresolved craters. Their abundance is roughly consistent with that expected for the continual impact of comets during the last 3 to 4 billion years.

The nature of the flows on both Ariel and Titania is uncertain. Water ice, which is thought to be a major component of the satellites, has a melting point some 200 K higher than the ambient surface temperatures. Ammonia–water ice mixtures, however, have a eutectic melting point 173 K lower and may be more likely sources of fluid in the Uranian satellites (*55*). Other volatile assemblages, such as methane or carbon monoxide clathrates, may also play a role in low-temperature resurfacing processes. The higher density of the Uranian satellites relative to the Saturnian satellites suggests greater radiogenic heating. Despite their greater heliocentric distance, the Uranian satellites have lower albedos that yield surface temperatures comparable to those of the Saturnian satellites. Because the sizes of the satellites and the upper boundary conditions are similar in the two systems, a greater fraction of radiogenic-bearing material implies higher internal temperatures, perhaps allowing low melting point condensates to provide the fluids necessary to resurface these objects. In addition, recent reviews of the dynamical history of the satellite orbits suggest that tidal resonances could have been important for heating Ariel at some time in the past (*41*).

Miranda. Miranda is the innermost of the major Uranian satellites; it is also the smallest. Its surface consists of two strikingly different major types of terrain: an old, heavily cratered, rolling terrain with relatively uniform albedo; and a young, complex terrain characterized by subparallel sets of bright and dark bands, scarps, and ridges in three regions that are trapezoidal to ovoid in shape (Fig. 27). The trapezoidal region (about 200 km on a side) occurs near the south pole and is located near the center of the mosaic shown in Fig. 27A; we informally refer to this feature as the "trapezoid." The trapezoid's outer boundary and its internal patterns of ridges and bands of contrasting albedo display numerous sharp corners.

Another region of complex terrain, illustrated on the right side of the geologic sketch map (Fig. 27B), is in the leading hemisphere. It is about 300 km wide in the direction parallel to the equator, but the other dimension is unknown because the terrain extends over the limb. The outer margin of this region, although somewhat rectangular in plan, has rounded corners and dark bands parallel with the boundary that curve smoothly around a more sharply rectangular core; we refer to this feature as the "banded ovoid." The highest contrast in albedo on Miranda's surface occurs in the trapezoid and banded ovoid.

A third region of complex terrain, referred to as the "ridged ovoid," occurs in the trailing hemisphere and was observed along the terminator (to the left in Fig. 27A). It is somewhat similar to the banded ovoid in

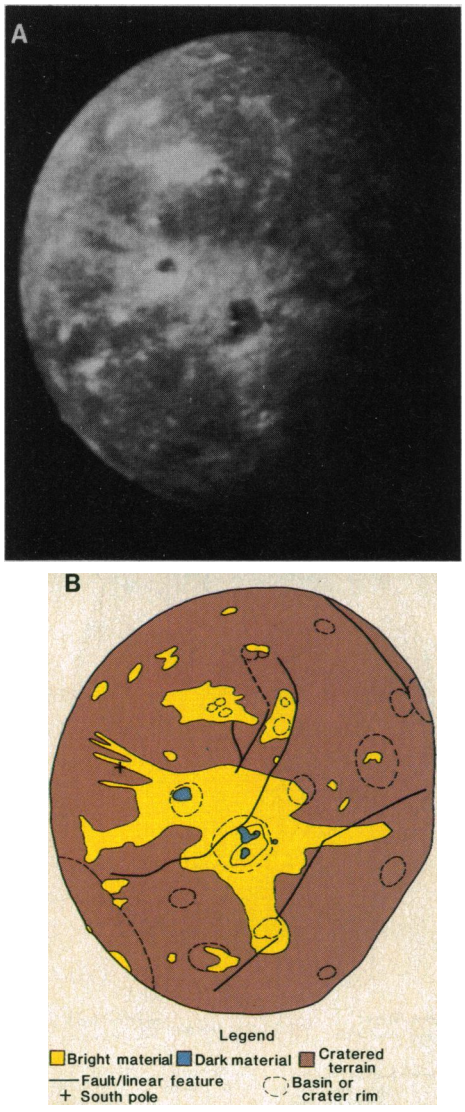

Fig. 22. (A) Voyager 2's highest resolution view of Oberon. This image was produced by summing two clear-filter images to improve the signal-to-noise ratio. The resultant image was processed to enhance details. The resolution is about 12 km per line pair, and the phase angle is about 45°. (B) Geologic sketch map of Oberon.

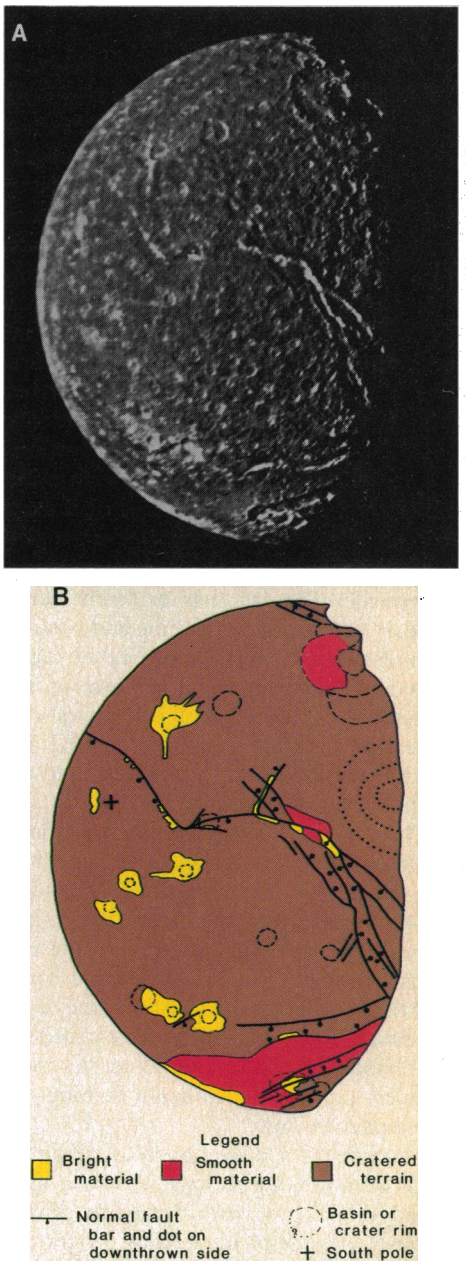

Fig. 23. (A) Voyager 2's highest resolution view of Titania. This image was high-frequency filtered to enhance details. The resolution is about 7 km per line pair, and the phase angle is about 35°. (B) Geologic sketch map of Titania.

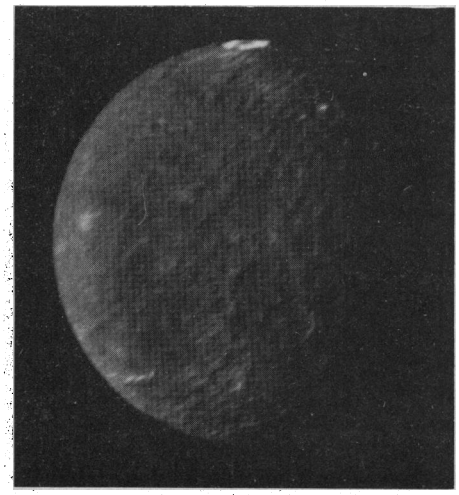

Fig. 24. Voyager 2's highest resolution view of Umbriel. This image was processed to enhance details. The resolution is about 11 km per line pair, and the phase angle is about 45°.

observed outline, size, and internal structure. Both the ridged and banded ovoids have an outer belt approximately 100 km wide, resembling a race track in form, that wraps around an inner core. The topography of the inner core of the ridged ovoid consists of a complex set of intersecting ridges and troughs that are truncated by the outer belt. The outer belt is marked by roughly concentric linear ridges and troughs and also includes small segments of the undulating cratered terrain. The ridge-and-trough belt somewhat resembles segments of grooved terrain on the Jovian satellite Ganymede. The belt has evidently developed at least in part by faulting and possibly by intrusion and extrusion of fluid or plastic material. An enlargement of part of the ridged ovoid (Fig. 28, A and B) shows what appear to be flows that have erupted and partly buried the grooves and ridges in the central core and outer band.

The dark bands along the outer margin of the banded ovoid correspond to outward-facing scarps (Fig. 29A), several of which appear to have slope widths of about 5 km. Because of the close similarity of the two ovoids in overall scale, planimetric form, and organization, we suggest that they were produced by variants of the same processes. The banded ovoid may be somewhat more evolved, perhaps by late-stage doming and subsequent collapse.

Many features in the trapezoid are similar to those in the ridged ovoid. An outer band of ridges and grooves wraps partly around an angular core of intersecting ridges and grooves in the interior of the trapezoid (Fig. 29B). This outer band, although much narrower than that in the ridged ovoid, sharply truncates ridges and grooves of the inner core. The terrain in the trapezoid was probably produced by many of the same geologic processes that shaped the ridged ovoid.

Other striking landforms on Miranda are enormous fault scarps that can be traced across the globe. Some of these are older than the trapezoid and the ovoids; others are younger. The most spectacular fault system begins at a deep valley visible at the terminator (Fig. 29C) and extends along the margin of the trapezoid and over the limb, where it forms a deep gorge on the outer margin of the banded ovoid. Near the terminator and bright limb, the fault system forms complex grabens. The highest fault scarps have slope widths of about 20 km; the graben seen on the bright limb (Fig. 29A) is 10 to 15 km deep.

Although most albedo contrast is found in the trapezoid and ovoid regions, some occurs also in the rolling cratered plains. Bright material is exposed in the upper parts of the walls of several impact craters and along fault scarps near the banded ovoid and the trapezoid. In places this bright material extends to depths of at least 1 km beneath the average level of the rolling cratered surface. In one location, adjacent to the banded ovoid and trapezoid, dark material is also exposed in craters and along scarps in the cratered terrain.

Most of the brightest material on Miranda's surface is found in impact craters in the trapezoid and the ovoids; it is present on the outer margin of the ridged ovoid, in the center of the banded ovoid, and in numerous places in the trapezoid. It may be that ice in the subsurface in these regions is brighter and cleaner than that beneath the cratered plains. Very dark materials are found primarily where the trapezoid and the banded ovoid have been breached by faults, exposing subsurface material.

Discussion of the satellite system. Collisions with short-period comets probably dominate the present production of craters on the Uranian satellites. This modern population was referred to as Population III in the analysis of the Saturnian satellite data (*53*). From the flux of long-period comets in its neighborhood, each giant planet captures a family of comets into short-period orbits. The annual flux of long-period comets at the orbit of Uranus, estimated by extrapolation from the flux observed near Earth, is about four times the flux at the orbit of Jupiter and about twice the flux at the orbit of Saturn. From theoretical studies (*59*) of the efficiency of capture of comets to short-period orbits, short-period comets of the Uranian family are estimated to be 600 to 700 times more numerous than those of the Jupiter family and about 100 times more numerous than those of the Saturn family. These high ratios are largely due to the long dynamical lifetimes of the Uranus family of comets. We estimate that the Uranus family of comets contains about 10^6 comet nuclei that are brighter than absolute B magnitude 18.

Table 3 gives our estimate, based on methods described earlier (*60*), of the present cratering rate on the Uranian satellites by impact of comet nuclei. Despite the large population, the Uranus-family comets are distributed over a much larger volume of space than the Jupiter and Saturn families of comets; hence, the present collision and cratering rates on the large Uranian satellites are comparable with the rates on the satel-

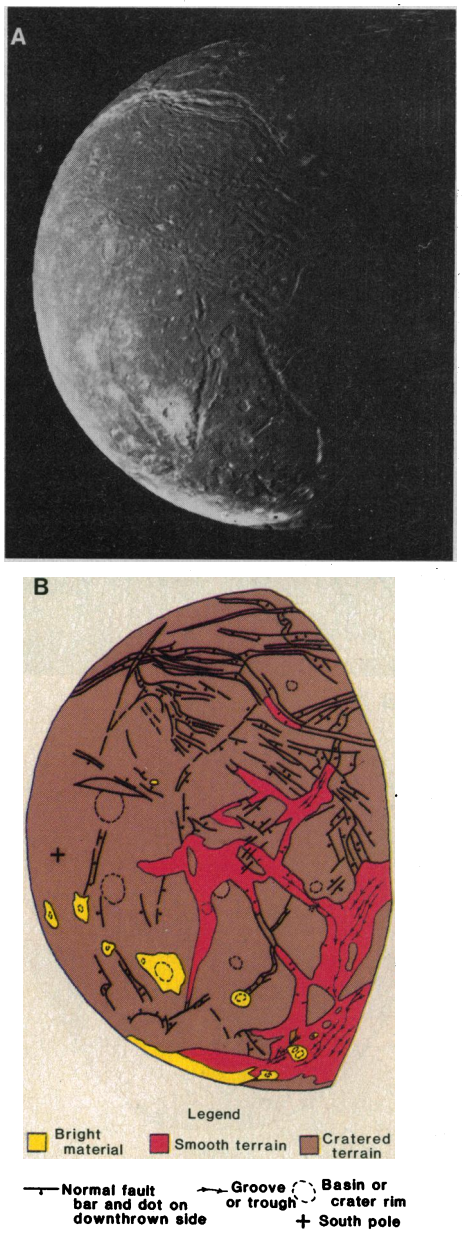

Fig. 25. (A) Mosaic of Voyager 2's highest resolution images of Ariel. The four images were acquired at a phase angle of about 60° with a resolution of about 2.5 km per line pair. The images along the terminator were somewhat smeared and are of lower effective resolution. (B) Geologic sketch map of Ariel.

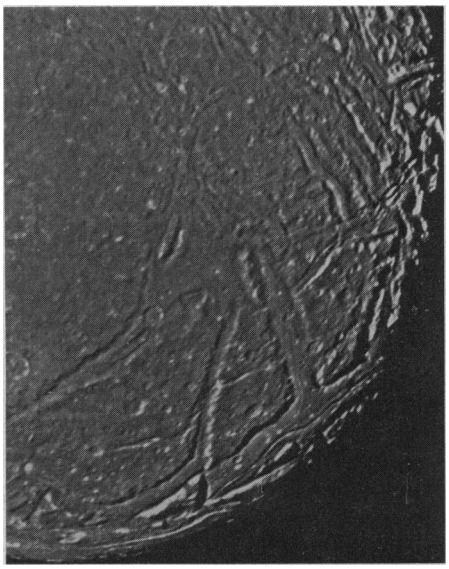

Fig. 26. Enhanced view of Ariel's terminator region. This view was assembled from several narrow-angle images acquired with the violet, blue, and green filters. The images were combined to provide the best unsmeared view of this region. The resolution is about 3.5 km per line pair. Fine detail has been exaggerated, particularly near the terminator.

lites of Jupiter. Because of the low orbital velocities of short-period comets at the distance of Uranus and the proximity of the Uranian satellites to the planet, the cratering rate from the outermost to the innermost satellites shows a strong gradient (Table 3). This gradient is due chiefly to the concentration of the comet flux in the Uranian gravity field. For example, the present cratering rate on the satellite orbiting just inside the ϵ ring is estimated to be more than 100 times higher than that for Oberon.

Craters observed on the heavily cratered surfaces of all the large Uranian satellites (Fig. 21) are far too abundant to be explained by steady bombardment at the estimated impact cratering rate over the last 3 to 4 billion years. Most of these craters must have been produced by impact of other objects early in the history of the solar system ($\sim 4 \times 10^9$ years ago) either by Uranus and Neptune planetesimals (Population I), or by small objects orbiting within the Uranian system (Population II), or, most probably, by both classes of objects. All craters observed on 1985U1, on the other hand, can be accounted for by comet impact at the present rate over the last several billion years.

We have also estimated (Table 3) the net cratering that each satellite would have undergone during the formation of the large Population I craters recorded on Oberon. As deduced for most of the satellites of Saturn (*53*), the Uranian satellites probably underwent intense collisional evolution during that period. If the craters on Oberon were produced by impact of Population I projectiles in heliocentric orbit (that is, by Uranus-Neptune planetesimals), then it is likely that some and perhaps all of the large satellites were disrupted by collision early in the history of the solar system. About five times as many craters as observed on Oberon would have been formed on Ariel and about 14 times as many on Miranda (Table 3). If the frequency of diameters of impacting projectiles was distributed roughly as a power function of size with an exponent near -2 [as derived for comet nuclei (*60*)], then Miranda probably was catastrophically disrupted and reaccreted several times by impact of objects large enough to produce a crater equal to or larger than the diameter of the satellite. Ariel was probably disrupted and reaccreted at least once; Umbriel may have been disrupted once. There is a fair chance that Titania was also disrupted. The abundant Population II craters could reflect the last stages of reaccretion of debris from a prior catastrophic disruption, from breakup of another satellite (such as a Trojan) in the orbit of Titania, or from a large impact on Titania itself.

At the present estimated flux of comets, the time scale for catastrophic collisional disruption of all the newly discovered satellites inside the radius of 1985U1 is about 2×10^9 years or less; the lifetime of the satellite discovered inside the radius of the ϵ ring is estimated to be about 10^9 years. For all these small satellites, the threshold for collisional disruption is taken to be equivalent to the energy required to produce a crater having a diameter equal to the radius of the satellite. The observed small satellites may have accreted from fragments derived from collisional disruption of 1985U1 a few billion years ago. Most of them may have been broken and reaccreted one or two times since then (Table 3). If small, undiscovered shepherding satellites are associated with any of the previously known narrow rings, the estimated collisional lifetimes of these satellites is a few hundred million years or less. Large (meter-size) ring particles may have collisional lifetimes of a few million years; it is very likely that the structure of the rings has not been static. Rings are probably continually produced by fragmentation of satellites that have been formed, in turn, by fragmentation of even larger objects. The history of ring evolution is very sensitive to the current impact flux; for instance, a flux five times lower than we estimate above would result in stable ring structure over geologic time.

The satellites of the outer solar system are, in general, mixtures of rock and ice in varying proportions. The chemical background for understanding such satellite compositions has been discussed by Lewis (*61*), who related the compositions and densities of planets and satellites to chemical-equilibrium condensation from the solar nebula. Later work by Lewis and others (*62*) has refined these ideas and extended them to nonequilibrium conditions, to various postulated solar nebula models, and to different conditions within protoplanetary nebulae. All these models require that the material that formed at Jupiter's orbit and beyond contain approximately equal amounts of silicate (commonly hydrated, at least initially) and water ice. At greater distances, more

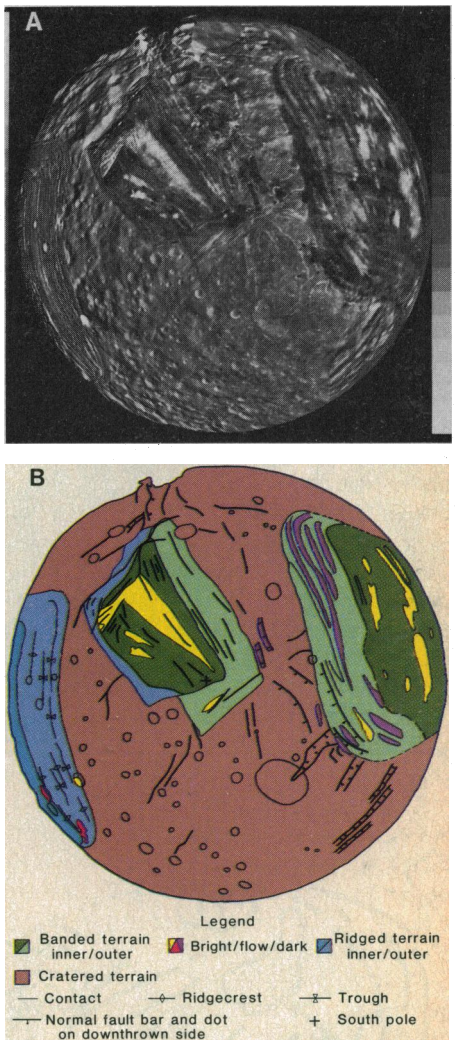

Fig. 27. (A) Mosaic of high-resolution images of Miranda. One wide-angle and eight narrow-angle camera images of Miranda were combined in this view. The controlled mosaic was transformed to an orthographic view centered on the south pole. Uranus is at the top; the apex of motion of the satellite is to the right in this view. The resolution of these images is about 0.6 km per line pair; the phase angle ranges from about 16° to 42°. [Digital cartography and image processing by K. Edwards, K. F. Mullins, and C. E. Isbell under the direction of R. W. Batson] (B) Geologic sketch map of Miranda.

volatile species may be present, particularly ammonia hydrate and methane clathrate ($CH_4 \cdot 6H_2O$), and eventually pure methane-ice.

The possible abundance of ammonia and methane compounds in the icy portions of these satellites is important for two reasons. First, the eutectic melting point of a mixture of ammonia and water ice is much lower than that for pure water ice, leading to the possibility of significant geologic activity even on small satellites (*55*). Second, methane ices, including methane clathrate with low ($\leq$1 to 200) occupancy ratios, have been shown in the laboratory to darken significantly under various types of irradiation (*63*), and the dark residues have been proposed as candidates for the dark material seen on surfaces such as those of Iapetus and the dark Uranian rings (*64*).

The amount of methane and ammonia incorporated in satellite materials depends strongly on the conditions in the nebular gas from which the material condensed. Recent theoretical work has suggested that the major carbon and nitrogen species in even the outer solar nebula may have been carbon monoxide and molecular nitrogen, not methane and ammonia, because of the effects of kinetic inhibition and turbulent transport in the nebula; on the other hand conditions in protoplanetary subnebulae might have favored methane and ammonia (*62*). Satellite densities are strongly affected by these differences because a nebula rich in carbon monoxide also has a lower water abundance: a satellite composed of rock, water ice, ammonia, and methane hydrate or clathrate should have an uncompressed density of about 1.25 g cm^{-3}; one composed of rock, water, and carbon and nitrogen clathrates should have a density of 1.7 to 1.8 g cm^{-3} (*55*).

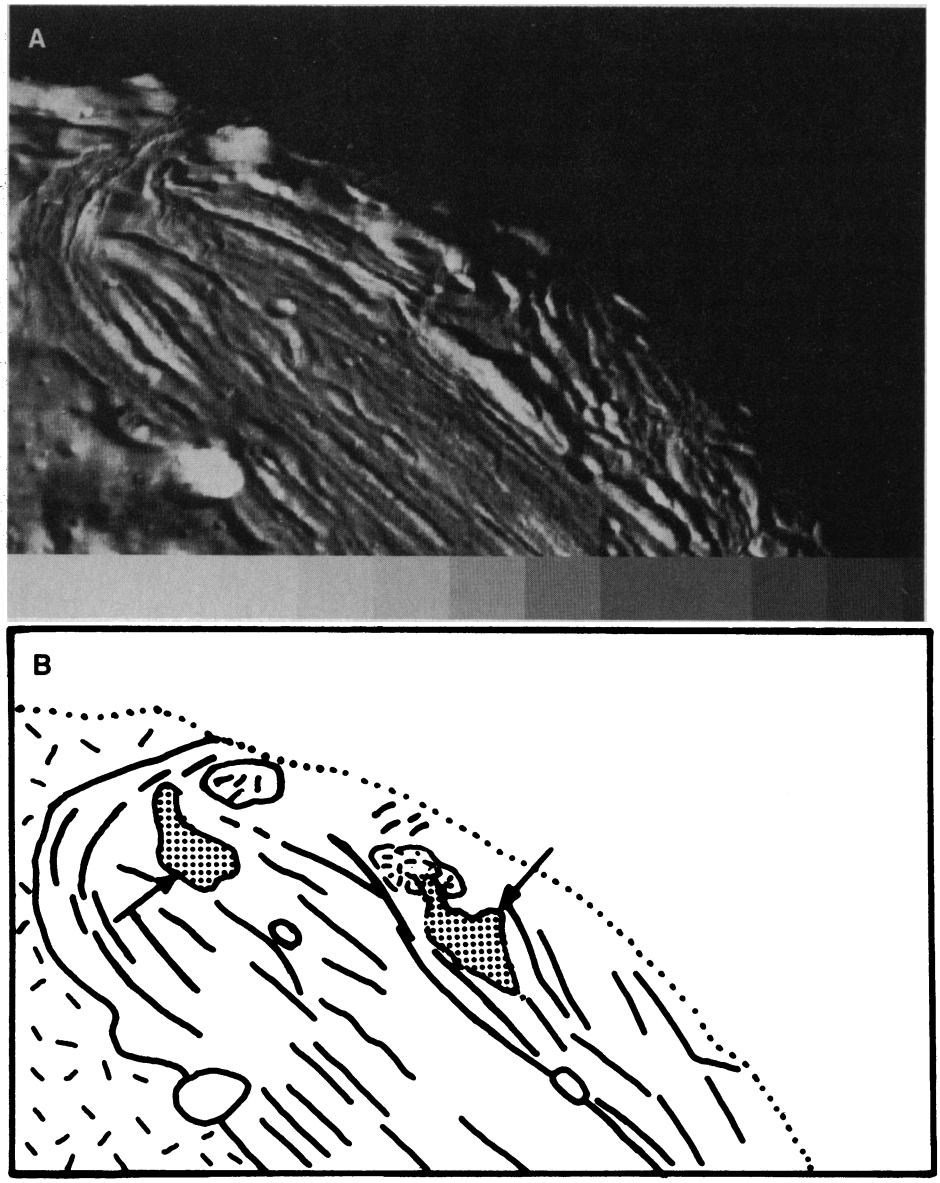

Fig. 28. (A) View of Miranda showing possible volcanic flows near the terminator in the ridged ovoid. (B) Sketch map of (A). Possible flows are indicated by arrows.

Although density does not uniquely determine bulk composition, several conclusions can be drawn from the densities of the satellites. First, all the satellites' densities (except Miranda's) are significantly heavier than those of the icy satellites of Saturn; only Dione has a density within the error limits of the outer four Uranian satellites (Fig. 16). Second, the satellites' mean density is too high to be modeled easily as an equilibrium condensation mixture of rock, water, and ammonia and methane compounds but at the same time too low to be completely compatible with estimated properties where all the carbon is in the form of carbon monoxide. Individual satellites, however, have values that might be compatible with either situation within the stated errors. We are left, then, with the possibility that the satellites' compositions are not related to a single equilibrium assemblage of either type; if they are so related, that assemblage seems to be closer to that expected from material rich in carbon monoxide but poor in water. A carbon monoxide–rich nebula would also affect the composition of material forming Uranus, raising further questions. Further, we must take into account the strong possibility that satellite formation conditions were affected by the event that created Uranus' large obliquity. Stevenson (*55*) pointed out that a circum-Uranian disk of material thrown out by a large-scale impact might contain shocked atmospheric material, which could also be water-poor.

The implications of the satellites' bulk compositions for their subsequent geologic and geophysical evolution are complex. Their densities imply relatively large rock fractions, which would mean that radiogenic heating may play a larger role in these satellites than in the Saturnian satellites. On the other hand, the possible lack of ammonia hydrate in the ice fraction would make melt conditions more difficult to reach within these fairly small bodies (*55*). The lack of extensive, geologically recent resurfacing on Umbriel, Titania, and Oberon is generally consistent with a low abundance of ammonia and methane, although Titania, the densest of the satellites, shows signs of resurfacing and tectonic activity that are at least comparable to those seen on Saturn's satellite Dione. Ariel and Miranda, on the other hand, show evidence of extensive resurfacing activity at some time in their history. They may have incorporated a greater fraction of low-melting-point ammonia hydrate or they may have been subjected to other sources of heat to trigger the observed

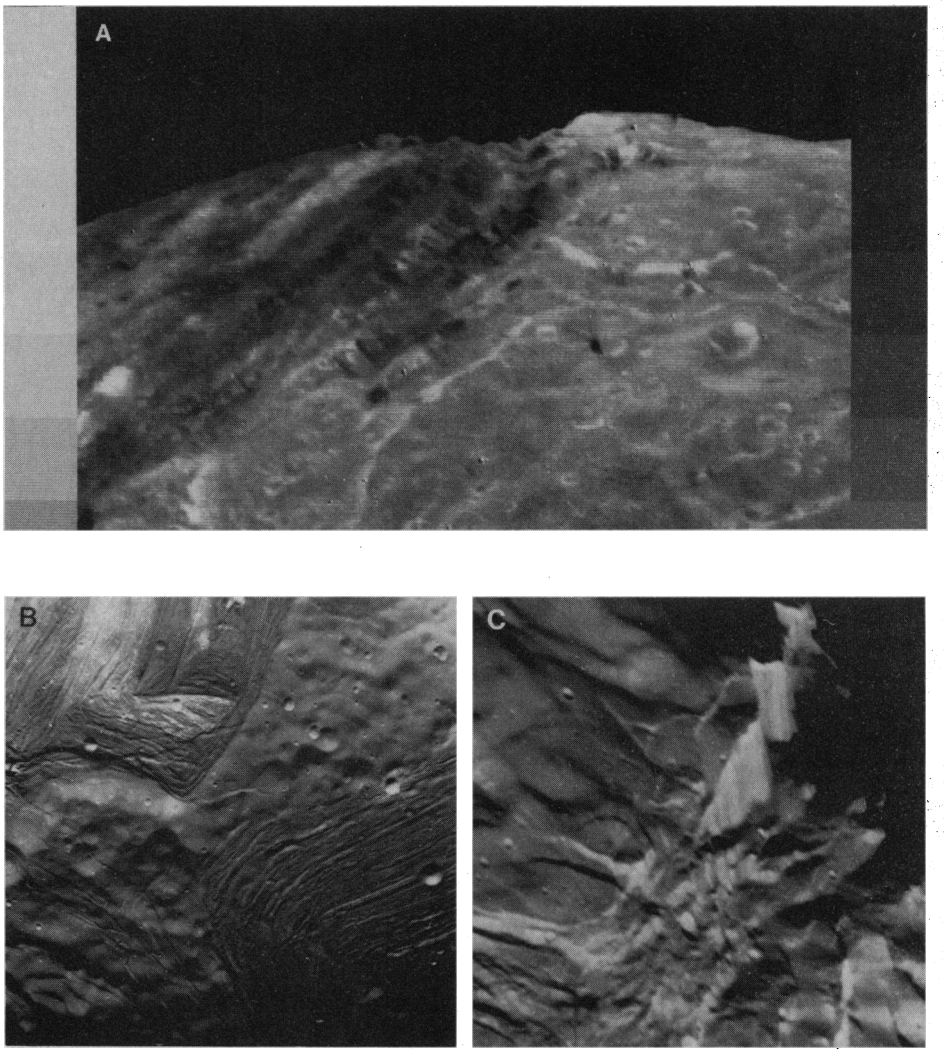

Fig. 29. (A) View of Miranda showing light- and dark-banded scarps near the boundary of the banded ovoid and a deep graben that bounds the ovoid in this region. (B) The angular inner cores and outer bands that wrap around them in the trapezoid and ridged ovoid regions. (C) The deep graben-like structure and enormous scarps at Miranda's terminator.

activity (or both). Although the Uranian satellites are not now in an orbital resonance similar to the LaPlace resonance among the Galilean satellites or the Dione-Enceladus resonance in the Saturnian system, their relatively large eccentricities and Miranda's inclination may indicate a complex orbital evolution, perhaps involving significant tidal heating, particularly for Ariel and possibly for Miranda (*41*).

The composition of the dark material and its relation to dark material found elsewhere in the solar system are major issues. The dark materials on the satellites and rings of Uranus display similar properties throughout the Uranian system: a geometric albedo of about 0.05 and a neutral spectral reflectance. The brighter materials covering most of the large satellites' surfaces are consistent with a mixture of this dark component and water ice. These characteristics are distinctly different from the properties of most silicate materials or the dark red material found on some asteroids (the D class) (*65*) and the dark material on Iapetus (*64*).

It is not especially surprising to find dark material in the outer solar system; only relatively differentiated silicate material is

Table 3. Estimated rates of present cratering and past production of large craters on the satellites of Uranus. Symbols: $P > 10$ km, present production rate of craters larger than 10 km in units of 10^{-14} km^{-2} year^{-1}; D_{max}, diameter of the largest crater probably produced in the last 3.5×10^9 years; Fr_{sat}, number of craters with diameter larger than the radius of the satellite produced in the last 3.5×10^9 years; $D = 10$ km, number of craters 10 km or more in diameter per square kilometer that would have been produced while the present craters on Oberon were formed; $D = D_{sat}$, number of craters with diameter equal to that of the satellite that would have been produced during the formation of the observed craters on Oberon.

Object	Present rate			Oberon equivalent		Implications for impact history
	$P > 10$ km (10^{-14} km^{-2} year^{-1})	D_{max} (km)	Fr_{sat}	$D =$ 10 km (km^{-2})	$D = D_{sat}$	
Oberon	0.79	113	0.015	0.0024	0.28	Observed surface corresponds to early period of heavy bombardment
Titania	1.11	135	0.020	0.0034	0.39	Probability of disruption while Oberon's craters formed is approximately 0.4
Umbriel	2.6	153	0.050	0.0080	0.97	Probably disrupted and reaccreted while Oberon's craters formed
Ariel	4.3	188	0.082	0.0131	1.6	Probably disrupted and reaccreted at least once
Miranda	10.9	131	0.25	0.033	4.8	Disrupted and reaccreted five times while Oberon's craters formed
1985U1	31	79	0.9	0.096	17	Last disrupted about 3.5×10^9 years ago
1986U5	51	39	1.8	0.16	34	All these objects probably were derived from fragmentation of a 1985U1 precursor about 3.5×10^9 years ago; most probably were disrupted and reaccreted in the last (1 to 2) $\times 10^9$ years
1986U4	44	69	1.4	0.14	26	
1986U1	56	53	1.9	0.17	36	
1986U2	59	55	2.0	0.18	37	
1986U6	68	45	2.4	0.21	46	
1986U3	70	45	2.5	0.21	47	
1986U9	79	41	2.9	0.25	58	
1986U8	84	44	3.5	0.29	66	Probably produced by fragmentation of larger objects during the last (0.5 to 1) $\times 10^9$ years
1986U7	107	47	3.9	0.33	75	

normally bright, whereas unmodified low-temperature condensates should resemble primitive carbonaceous chondrites that contain quite dark spectrally neutral dark material. Such chondrites consist of a mixture of organics, opaque minerals (such as magnetite), and carbon. Even in these materials, however, there is usually some decrease in reflectance in the ultraviolet.

Pure carbon is another candidate for such materials. Among the asteroids, there are examples of both dark red and spectrally neutral bodies. In addition, laboratory studies of irradiated methane, including methane clathrate, show that after continued irradiation the dark red residue eventually becomes dark and spectrally flat. Although the exact chemical nature of this residue is not known, it most probably is enriched in pure carbon and polycyclic aromatic hydrocarbons (*63*). The characteristics of the spectra of the Uranian satellites are most similar to those of Phoebe at Saturn and the dark C-class asteroids.

The relations among the various types of dark materials in the outer solar system, from the asteroid belt outward, are not clear. Much of this material may be part of the primitive condensate from which the planets and satellites formed 4.5 billion years ago. Some of the dark material may also have been produced from irradiation of methane or methane clathrate at some undefined later epoch that may extend to the recent geologic past.

Thus, there are two ways to explain the nature of the dark material in this system, both of which have some interesting implications. (i) The material could be primarily radiation-darkened methane, probably in clathrate form. This implies that the primitive-appearing small satellites and Umbriel, with its heavily cratered surface, have more methane clathrate than the other satellites that not only display a greater degree of geologic activity but also exhibit some old, bright regions. It also implies that the satellites' compositions may be far from a single equilibrium mixture of silicate and ice. (ii) The material could be primarily primordial dark material. This is more in accord with the satellites' densities; however, it also implies a possible deficiency in available ammonia hydrate to facilitate geologic activity.

REFERENCES AND NOTES

1. J. Veverka, J. Goguen, S. Yang, J. Elliot, *Icarus* **34**, 406 (1978).
2. B. A. Smith *et al.*, *Space Sci. Rev.* **21**, 103 (1977); G. E. Danielson *et al.*, *J. Geophys. Res.* **86**, 8683 (1981). The Voyager images are radiometrically calibrated and expressed in terms of I/F, where I is the measured radiance in a particular spectral bandpass and F is the solar irradiance in the same bandpass.
3. J. T. Bergstralh and K. H. Baines, in *Uranus and Neptune*, J. T. Bergstralh, Ed. (*NASA Conf. Publ. 2330*, 1984), pp. 179–212.
4. J. B. Pollack *et al.*, *Icarus*, in press.
5. G. L. Tyler *et al.*, *Science* **233**, 79 (1986).
6. R. Hanel *et al.*, *ibid.*, p. 70.
7. B. J. Conrath *et al.*, *J. Geophys. Res.* **86**, 8769 (1981); J. A. Pirraglia *et al.*, *Nature (London)* **292**, 677 (1981); A. P. Ingersoll *et al.*, in *Saturn*, T. Gehrels and M. S. Matthews, Eds. (Univ. of Arizona Press, Tucson, 1984), pp. 195–238.
8. R. A. West, P. N. Kupferman, H. Art, *Icarus* **61**, 311 (1985).
9. K. Rages, J. B. Pollack, P. H. Smith, *J. Geophys. Res.* **88**, 8721 (1983).
10. F. Franklin *et al.*, *Astrophys. J.* **236**, 1031 (1980); J. Elliot *et al.*, *Astron. J.* **86**, 444 (1981).
11. A. P. Ingersoll *et al.*, *J. Geophys. Res.* **86**, 8733 (1981); L. A. Sromovsky *et al.*, *ibid.* **88**, 8650 (1983).
12. J. W. Warwick *et al.*, *Science* **233**, 102 (1986); N. F. Ness *et al.* (*25*).
13. P. L. Read, *Q. J. R. Meteorol. Soc.* **112**, 253 (1986).
14. J. R. Holton, *An Introduction to Dynamic Meteorology* (Academic Press, New York, ed. 2, 1979), pp. 68–71.
15. D. J. Stevenson, *Geophys. Astrophys. Fluid Dyn.* **21**, 113 (1982); ———, *Annu. Rev. Earth Planet. Sci.* **10**, 257 (1982); ———, private communication.
16. A. P. Ingersoll and D. Pollard, *Icarus* **52**, 62 (1982).
17. J. L. Elliot and P. D. Nicholson, in *Planetary Rings*, R. Greenberg and A. Brahic, Eds. (Univ. of Arizona Press, Tucson, 1984), pp. 25–72.
18. P. D. Nicholson and K. Matthews, *Bull. Am. Astron. Soc.* **15**, 816 (1983).
19. R. J. French, J. L. Elliot, S. E. Levine, *Icarus*, in press.
20. P. D. Nicholson, T. J. Jones, K. Matthews, *Proc. IAU Colloq.* **75**, 169 (1984).
21. R. J. Terrile and B. A. Smith, *Bull. Am. Astron. Soc.* **16**, 657 (1984).
22. J. N. Cuzzi, *Icarus* **63**, 312 (1985).
23. The reflectivity I/F of a ring of finite normal optical depth τ is a function of τ, the cosines of the solar and spacecraft elevation angles μ_0 and μ, the value of the angular variation of scattered brightness, or phase function, of the particle $P(\theta)$ at phase angle θ, and the angle-integrated single-scattering albedo ω_0 (*22*). The reflectivity of an individual particle is the product $\omega_0 P(\theta)$. For low optical depths, the exact expression for I/F reduces to the product $\omega_0 P(\theta)\tau/4\mu$.
24. A. L. Lane *et al.*, *Science* **233**, 65 (1986).
25. N. F. Ness *et al.*, *ibid.*, p. 85.
26. A. L. Broadfoot *et al.*, *ibid.*, p. 74.
27. J. A. Burns *et al.*, *Nature (London)* **316**, 115 (1985).
28. P. Goldreich and S. Tremaine, *ibid.* **277**, 97 (1979).
29. C. Porco, thesis, California Institute of Technology (1983); L. W. Esposito *et al.*, *Science* **222**, 57 (1983); C. Porco *et al.*, *Icarus* **60**, 1 (1984).
30. J. N. Cuzzi *et al.*, in *Planetary Rings*, R. Greenberg and A. Brahic, Eds. (Univ. of Arizona Press, Tucson, 1984), pp. 73–199.
31. J. A. Burns *et al.*, *Icarus* **44**, 339 (1980); J. A. Burns *et al.*, in *Planetary Rings*, R. Greenberg and A. Branic, Eds. (Univ. of Arizona Press, Tucson, 1984), pp. 200–272.
32. J. A. Burns, personal communication.
33. S. F. Dermott and C. Murray, *Icarus* **48**, 1 (1981).
34. L. J. Horn, A. L. Lane, J. N. Cuzzi, *Bull. Am. Astron. Soc.* **17**, 717 (1985).
35. P. Goldreich and S. Tremaine, *Annu. Rev. Astron. Astrophys.* **20**, 249 (1982); J. Lissauer and J. N. Cuzzi, *Astron. J.* **87**, 1051 (1982).
36. J. N. Cuzzi and J. D. Scargle, *Astrophys. J.* **292**, 276 (1985).
37. P. Goldreich, personal communication.
38. C. Proco *et al.*, *Icarus* **60**, 17 (1984); N. Borderies, P. Goldreich, S. Tremaine, *Nature (London)* **299**, 209 (1982).
39. R. Greenberg, *Icarus* **24**, 325 (1975); *ibid.* **29**, 427 (1976); in *Dynamics of the Solar System*, L. Duncombe, Ed. (Reidel, Dordrecht, 1979), p. 177; in *Uranus and Neptune*, J. T. Bergstralh, Ed. (*NASA Conf. Publ. 2330*, 1984), p. 463; C. Veillet, thesis, University of Paris (1984); S. F. Dermott and P. D. Nicholson, preprint (1985).
40. R. H. Brown, in *Uranus and Neptune*, J. T. Bergstralh, Ed. (*NASA Conf. Publ. 2330*, 1984), p. 137; D. P. Cruikshank and R. H. Brown, in *Satellites*, J. Burns and M. S. Matthews, Eds. (Univ. of Arizona Press, Tucson, in presss).
41. S. Squyres, R. Reynolds, J. Lissauer, *Icarus* **61**, 218 (1985).
42. S. J. Peale, in *Planetary Satellites*, J. A. Burns, Ed. (Univ. of Arizona Press, Tucson, 1977), pp. 87–112.
43. R. H. Brown and R. N. Clark, *Icarus* **58**, 288 (1984).
44. R. H. Brown, D. P. Cruikshank, D. Morrison, *Nature (London)* **300**, 423 (1982).
45. D. P. Cruikshank, *Icarus* **41**, 246 (1980); ——— and R. H. Brown, *ibid.* **45**, 607 (1981).
46. B. T. Soifer, G. Neugerbauer, K. Matthews, *ibid.* **45**, 612 (1981).
47. R. H. Brown and D. P. Cruikshank, *ibid.* **55**, 83 (1983).
48. R. H. Brown, *ibid.* **56**, 414 (1983).
49. J. Laskar and C. Yoder, private communication.
50. J. Goguen, H. Hammel, R. H. Brown, *Icarus*, in press.
51. B. Hapke, *ibid.*, in press.
52. K. D. Pang and J. W. Rhoads, *Abstr. IAU Colloq.* **77**, 40 (1983); B. Hapke, *Bull. Am. Astron. Soc.* **15**, 856 (1983).
53. B. A. Smith *et al.*, *Science* **212**, 163 (1981); B. A. Smith *et al.*, *ibid.* **215**, 504 (1982).
54. K. E. Herkenhoff and D. J. Stevenson, *Abstr. Lunar Planet. Sci. Conf.* **15**, 361 (1984).
55. D. J. Stevenson, in *Uranus and Neptune*, J. T. Bergstralh, Ed. (*NASA Conf. Publ. 2330*, 1984), p. 405.
56. T. Owen, in *Ices in the Solar System*, I. P. Klinger *et al.*, Eds. (Reidel, Dordrecht, 1985), p. 731.
57. Q. R. Passey and E. M. Shoemaker, in *Satellites of Jupiter*, D. Morrison, Ed. (Univ. of Arizona Press, Tucson, 1982), p. 177.
58. Although Veillet (*39*) recently estimated masses from analysis of astrometric data, the errors in these estimates for the outer satellites were later found to be so large as to be indeterminate [S. F. Dermott and P. D. Nicholson, *Nature (London)* **319**, 115 (1986)].
59. E. Everhart, *Astrophys. J. Lett.* **10**, 131 (1972); E. Everhart, in *Comets, Asteroids and Meteorites*, A. H. Delsemme, Ed. (Univ. of Toledo Press, Toledo, OH, 1977), p. 99.
60. E. M. Shoemaker and R. F. Wolfe, in *Satellites of Jupiter*, D. Morrison, Ed. (Univ. of Arizona Press, Tucson, 1982), p. 277.
61. J. S. Lewis, *Icarus* **15**, 175 (1971).
62. J. S. Lewis and R. G. Prinn, *Astrophys. J.* **238**, 357 (1980); R. G. Prinn and B. Fegley, *ibid.* **249**, 308 (1981).
63. G. Strazzulla, L. Calcagno, G. Foti, *Mon. Not. R. Astron. Soc.* **204**, 59 (1983); L. Calcagno, G. Foti, L. Torrisi, G. Strazzulla, *Icarus* **63**, 31 (1985); L. J. Lanzerotti, W. L. Brown, R. E. Johnson, in *Ices in the Solar System*, J. Klinger, Ed. (Reidel, Dordrecht, 1985), p. 317; A. R. Cheng, in *Uranus and Neptune*, J. T. Bergstralh, Ed. (*NASA Conf. Publ. 2330*, 1984), p. 541; W. R. Thompson, B. G. J. P. T. Murray, B. N. Khare, C. Sagan, preprint (1986).
64. D. P. Cruikshank *et al.*, *Icarus* **53**, 90 (1983); S. W. Squyres and C. Sagan, *Nature (London)* **303**, 782 (1983).
65. J. Degewij and C. J. Van Hooten, in *Asteroids*, T. Gehrels, Ed. (Univ. of Arizona Press, Tucson, 1979), p. 417.
66. M. J. Lupo and J. S. Lewis, *Icarus* **44**, 41 (1980).

67. We thank the Voyager spacecraft team for their outstanding efforts in reducing camera smear; A. Hartch for her efforts in preparing the encounter sequence; D. Hinson for his help in the design of the high phase angle ring observation during the limb-track maneuver; M. Ockert, B. Mostert, J. Gotobed, and B. Owens for valuable technical support; M. Showalter, L. Dones, L. Doyle, J. Spencer, and D. Grinspoon for their assistance during encounter; D. A. Alexander, G. W. Garneau, E. P. Korsmo, S. K. LaVoie, H. B. de Rueda, S. T. Rifke, J. S. Shiflet, C. L. Stanley, E. T. Wachner, and L. A. Wainio, under the able direction of C. C. Avis, for image processing support through the encounter; R. M. Batson, P. M. Bridges, K. Edwards, E. M. Eliason, J. L. Inge, C. E. Isbell, K. F. Mullins, and T. L. Rock for cartographic and image processing support; J. A. Burns, P. Goldreich, F. Shu, P. D. Nicholson, C. Leovy, and D. J. Stevenson for helpful reviews and comments; R. A. Jacobson for assistance in developing the numerically integrated model of the ephemerides of the Uranian satellites and its application to fitting both the long intervals of Earth-based astrometric measurements and the Voyager optical data; R. F. Wolfe for her contributions to calculations of current Uranian cometary fluxes and the early collisional histories for the satellites; J. L. Anderson for coordination of the production of all imaging data products; E. Simien and E. Edwards for maintaining the Voyager Imaging Team data libraries; and D. Weir and S. Bounds for editorial assistance.

8 April 1986; accepted 5 May 1986